CLOUD CONDENSATION NUCLEI SPECTRA: MEASUREMENT TECHNIQUES AND AMBIENT SAMPLING IN THE SOUTHEASTERN UNITED STATES

BY JACK J. LIN

A Thesis
Presented to
The Academic Faculty

by

Jack J. Lin

In Partial Fulfillment
of the Requirements for the Degree
Doctor of Philosophy in the
School of Earth and Atmospheric Sciences

Georgia Institute of Technology
August 2016

CLOUD CONDENSATION NUCLEI SPECTRA: MEASUREMENT TECHNIQUES AND AMBIENT SAMPLING IN THE SOUTHEASTERN UNITED STATES

BY JACK J. LIN

Approved by:

Athanasios Nenes, Advisor
School of Earth and Atmospheric Sciences
Georgia Institute of Technology

Yuhang Wang
School of Earth and Atmospheric Sciences
Georgia Institute of Technology

Nga Lee Ng
School of Chemical and Biomolecular Engineering
Georgia Institute of Technology

Rodney J. Weber
School of Earth and Atmospheric Sciences
Georgia Institute of Technology

Armistead G. Russell
School of Civil and Environmental Engineering
Georgia Institute of Technology

Date Approved: 17 May 2016

ACKNOWLEDGEMENTS

It takes a village to raise a child goes the old proverb. The same is true for academic affairs. I have stood on the shoulders of many people, and the view has been quite nice.

TABLE OF CONTENTS

LIST OF TABLES

LIST OF FIGURES

SUMMARY

Atmospheric aerosols take part in many processes that affect Earth's climate. These interactions are highly complex, and their imperfect representations in global climate models lead to a high amount of uncertainty in our estimates of the anthropogenic impact on climate change. Measurements of the ability of aerosols to act as cloud condensation nuclei (CCN) continue to be necessary to improve our understanding of the interaction between aerosols and clouds. In this thesis, instrument technique development for the fast measurement of CCN spectra and ambient measurements of aerosol properties in the southeastern United States are presented.

Scanning Flow CCN Analysis (SFCA) allows for the measurement of CCN spectra with high resolution in space, time, and supersaturation. Hardware improvements in the form of an Arduino microcontroller and a mass flow controller (MFC) have increased the robustness and flexibility of the measurements. The supersaturation generated during SFCA operation was comprehensively characterized. A set of calibration experiments and instrument model simulations were used to assess the performance of SFCA for a wide range of operating conditions, including instrument pressure, flow rate waveform, and flow rate period for both laboratory and ambient sampling conditions.

The Arduino+MFC module has been flown on four airborne field deployments to good results. The results from the SENEX field campaign are presented here. SENEX was a part of the Southeast Atmosphere Study (SAS), a broad effort in the summer of 2013 to comprehensively characterize the meteorology, chemistry, and aerosol in the southeastern United States. SAS was partly motivated by the anomalous cooling trend observed in the southeastern United States over the past fifty years. Aerosol size and composition, CCN activity, and cloud droplet number where characterized from data measured aboard the National Oceanic and Atmospheric Administration (NOAA) WP-3D aircraft and evaluated

against simulations using the Community Atmosphere Model (CAM) and Community Multi-scale Air Quality Model (CMAQ). Aerosol in the southeastern United States was found to mostly composed of organics, but the composition of Aitken mode aerosol was found to have hygroscopicity similar to pure inorganic compounds. Both models fail to capture key characteristics of the observed aerosol. In particular, both models largely underestimating the total aerosol number. Under typical observed updraft values, however, the resulting cloud droplet number is only underestimated by a factor of two. Using the sensitivities of cloud droplet number to relevant input parameters, it was determined that the primary driver of discrepancy between the cloud droplet number computed from the observed and modeled aerosol parameters is the total aerosol number.

CHAPTER I

INTRODUCTION

Water vapor does not self-nucleate under atmospheric conditions. The time necessary to see one single water droplet self-nucleate under atmospheric conditions is longer than the age of the universe (John H. Seinfeld, personal communication, February 2009). Yet, some 5.7×10^{14} cubic meters of water per year manages to fall from the sky (*Legates and Willmott*, 1990). How can water and ice, both much more dense than air, float so serenely in the clouds in the sky?

1.1 Aerosols in the Earth System

Aerosols are atmospheric particles of natural or anthropogenic origin that arise directly from emissions or secondary conversion from the gas phase. They are highly variable in both time and space due to the meteorology, primary emissions, and precursor emissions that govern their properties and quantity in the atmosphere. They can be present in the atmosphere at concentrations up to 10^8 cm^{-3} with diameters spanning orders of magnitude from 10^{-9}–10^{-4} m. Fine particles with diameters less than 1 μm have a lifetime in the atmosphere of days to weeks and can be transported 10^2–10^3 km, while coarse particles with diameters greater than 1 μm have a lifetime in the atmosphere of minutes to days and are transported less than 10 km (*Seinfeld and Pandis*, 2006).

Aerosols play important roles in many processes comprising the Earth system. They interact with solar radiation by absorption and scattering and interact to a lesser extent with terrestrial radiation by absorption, scattering, and emission. Aerosols play a role in the hydrological cycle through their ability to act as cloud condensation nuclei (CCN) ice nuclei (IN) and, to a lesser extent, by influencing the distribution and rate of precipitation. Aerosols play wider roles in atmospheric chemistry by serving as heterogeneous reaction sites (*George and Abbatt*, 2010) and in biogeochemical cycles as carriers of nutrients (*Andreae and Crutzen*, 1997).

1.2 Climatic Effects of Aerosols

Aerosols affect the global radiation balance via the so-called direct effect by scattering and absorbing solar radiation. Aerosols also influence the global radiation balance via the so-called indirect effect by acting as CCN and IN and modifying cloud microphysical properties. The large spatial and temporal variability of aerosols along with their relatively short atmospheric lifetime of aerosol particles means the effects of aerosol-cloud interactions (ACIs) on the climate system are some of the most uncertain components of anthropogenic climate forcing (*Ramanathan et al.*, 2001). The mechanisms in which aerosols indirectly modify Earth's radiative balance are shown in Figure 1.1

An increase of aerosol particles in a cloud with the same liquid water content (LWC) produces a cloud with more numerous, smaller cloud droplets compared to an unperturbed cloud. The smaller, but more numerous, cloud droplets create a brighter cloud that is more reflective of shortwave radiation from the sun. This is known as the cloud albedo effect or

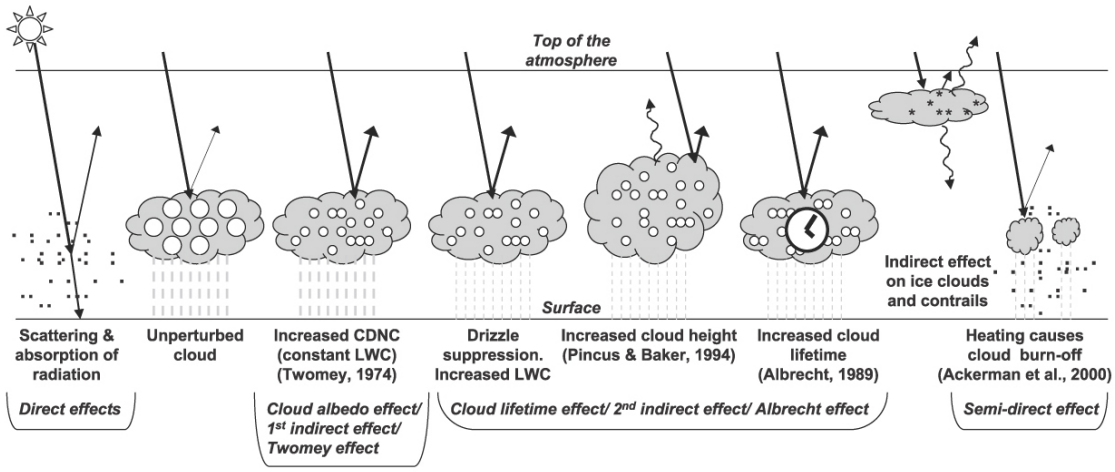

Figure 1.1: Schematic diagram showing the various radiative mechanisms associated with cloud effects that have been identified as significant in relation to aerosols (modified from Haywood and Boucher, 2000). The small black dots represent aerosol particles; the larger open circles cloud droplets. Straight lines represent the incident and reflected solar radiation, and wavy lines represent terrestrial radiation. The filled white circles indicate cloud droplet number concentration (CDNC). The unperturbed cloud contains larger cloud drops as only natural aerosols are available as cloud condensation nuclei, while the perturbed cloud contains a greater number of smaller cloud drops as both natural and anthropogenic aerosols are available as cloud condensation nuclei (CCN). The vertical grey dashes represent rainfall, and LWC refers to the liquid water content. Figure and caption reproduced with permission from Figure 2.10 of *Forster et al.* (2007).

first indirect effect or Twomey effect (*Twomey*, 1974, 1977). Aerosols have a number of other influences on cloud properties referred to collectively as the cloud lifetime effect or second indirect effect or Albrecht effect. Smaller cloud droplets in a cloud perturbed by additional aerosol particles are less likely to grow to large enough sizes to initiate precipitation. This leads to an increase in the LWC of the cloud and an increase in the lifetime of the cloud through the suppression of drizzle (*Albrecht*, 1989). The suppression of drizzle and increase lifetime allows the cloud to grow to taller heights, further modifying cloud albedo (*Pincus and Baker*, 1994).

The Fourth Assessment Report (AR4) of the Intergovernmental Panel on Climate Change (IPCC) estimated the median cloud albedo radiative forcing[1] to be -0.7 W m^{-2} with a 5–95% range of -0.3 to -1.8 W m^{-2} with low level of scientific understanding. In the Fifth Assessment Report (AR5), aerosol radiative impacts were assessed in terms of effective radiative forcing (ERF)[2]. By allowing atmospheric variables to adjust to perturbations, ERF gives a more accurate representation of the temperature response to those perturbations. AR5 found the ERF from aerosol-cloud interactions to be -0.45 W m^{-2} with a 5–95% range of -1.20 to 0.00 W m^{-2}. Including the radiative forcing from rapid adjustments in aerosol-radiation interactions gives an integrated component of adjustment due to aerosols of -0.55 W m^{-2} with a 5–95% range of -1.33 to -0.06 W m^{-2} with low level of confidence (*IPCC*, 2013; *Stocker et al.*, 2013). While ERF gives a better representation of the temperature response to ACIs compared to RF, progress between AR4 and AR5 has been slow with the estimate of the radiative impact due to ACIs still having a low level of confidence.

While progress has been made in our understanding of aerosol impacts on climate, the quantification of aerosol-cloud interactions in climate models continues to be a challenge and confidence in the representation of aerosol processes in climate models remains weak. Aerosol and cloud processes take place on spatial scales significantly smaller than those

[1]Radiative forcing is defined in the IPCC (*Myhre et al.*, 2013) as "the change in net downward radiative flux at the tropopause after allowing for stratospheric temperatures to readjust to radiative equilibrium, while holding surface and tropospheric temperatures and state variables such as water vapor and cloud cover fixed at the unperturbed values."

[2]Effective radiative forcing is defined in the IPCC as the change in net TOA downward radiative flux after allowing for atmospheric temperatures, water vapor, and clouds to adjust, while holding the properties of oceans and ice cover constant (*Myhre et al.*, 2013).

climate models are currently able to resolve. Until the various aerosol-cloud interactions are fully represented by sub-grid scale parameterizations, estimates of the radiative impacts of aerosol-cloud interactions will continue to be highly uncertain (*Boucher et al.*, 2013).

1.3 Aerosols as Cloud Condensation Nuclei

Atmospheric aerosols serve as the surfaces upon which atmospheric water vapor may condense. The thermodynamics of aqueous solution drops are governed by Köhler Theory (*Köhler*, 1936). The equilibrium between the water droplet solution and water vapor is expressed as

$$\log\left[\frac{p_w\left(D_p\right)}{p^\circ}\right] = \frac{4M_w\sigma_w}{RT\rho_w D_p} - \frac{6n_s M_w}{\pi\rho_w D_p^3} \tag{1}$$

where $p_w\left(D_p\right)$ is the vapor pressure of water over a surface of diameter D_p; p° is the vapor pressure of water over a flat surface; M_w is the molecular weight of water; σ_w is the surface tension of water; ρ_w is the density of water; and n_s is the moles of solute. The ratio p_w/p° is the saturation, S, relative to a flat pure water surface required for droplet equilibrium. When $S > 1$, the term supersaturation, s, is used with $s \equiv S - 1$. Often, the supersaturation is expressed as a percentage with $ss\% = s/100$. Equation 1 encompasses two competing effects that define the equilibrium vapor pressure over an aqueous solution droplet—the Kelvin, or curvature, effect that increases vapor pressure and the Raoult, or solute, effect that decreases vapor pressure. Example Köhler curves are shown in Figure 1.2. All the curves in Figure 1.2 contain a maximum occurring at a critical droplet diameter D_{pc} and critical saturation S_c. Once a particle's environment exceeds its critical saturation, the particle becomes thermodynamically unstable and grows rapidly into a cloud droplet. The particle is said to have activated and is defined as a CCN at that critical supersaturation.

Köhler Theory may be extended to include scenarios such as drops containing an insoluble substance (*Kokkola et al.*, 2008), adsorption of water onto insoluble substances (*Sorjamaa and Laaksonen*, 2007; *Kumar et al.*, 2009), drops containing slightly soluble substances (*Shulman et al.*, 1996; *Laaksonen et al.*, 1998), drops containing dissolved gases (*Kulmala et al.*, 1993; *Laaksonen et al.*, 1998), surfactant effects (*Shulman et al.*, 1996; *Facchini et al.*, 1999), and solute dissolution kinetics (*Asa-Awuku and Nenes*, 2007).

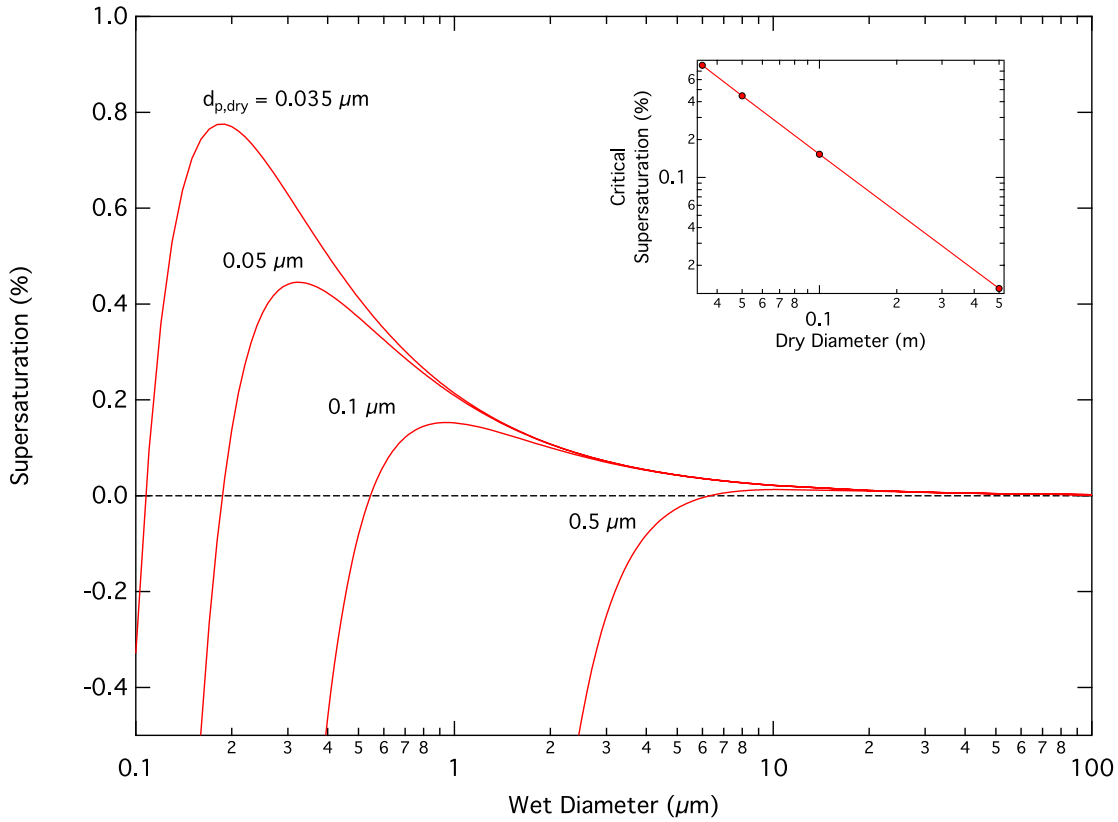

Figure 1.2: Köhler curves for ammonium sulfate particles of varying dry diameters. The relationship between dry diameter and critical supersaturation necessary for CCN activation is shown in the inset.

As evident from Köhler Theory, the ability of aerosol particles to act as CCN depends primarily on the size and composition of the particles and the ambient supersaturation (*Seinfeld and Pandis*, 2006). Due to the diversity of chemical species in the atmosphere and the complexities of aerosol formation and evolution pathways, aerosol size and chemistry are highly heterogeneous in both time and space. In particular, aerosol composition, especially the organic fraction, poses challenges in predictive models (*Volkamer et al.*, 2006). A single-parameter representation of Köhler Theory has been developed by *Petters and Kreidenweis* (2007) with the hygroscopicity parameter κ representing the compositional effects on dissolved solute in the droplet and the droplet surface tension. Expressed in terms of κ, the supersaturation a particle needs to be exposed to in order to act as a CCN is

$$s_c \approx \sqrt{\frac{4}{\kappa D_{p,dry}^3}\left(\frac{4\sigma M_w}{3RT\rho_w}\right)^3} \tag{2}$$

where $D_{p,dry}$ is the dry particle diameter. From Equation 2, we see that a dry size $D_{p,dry}$ and hygroscopicity κ will define a supersaturation at which a particle will act as a CCN. Alternatively, we may say that when particles with a given κ are exposed to some constant supersaturation, particles above some critical diameter $D_{c,dry}$ will act as CCN. Given measurements of CCN number concentration at a certain supersaturation and the particle size distribution, the critical diameter for the specified supersaturation may be found by integrating the particle size distribution to match the measured CCN concentration,

$$N_{CCN(s)} = \int_{D_{c,dry}}^{\infty} n_{CN} dD_p \tag{3}$$

where $N_{CCN(s)}$ is the measured CCN number concentration at supersaturation s and n_{CN} is the measured dry particle size distribution. Using Equation 2, the derived $D_{c,dry}$ may be related to a κ that describes the particle size distribution. Conversely, if the κ of a particle size distribution is known, Equation 2 may be used to predict the CCN number concentration at a given supersaturation. Comparison between predicted and measured CCN concentrations is known as CCN closure.

Estimates of the global distribution of aerosol hygroscopicity range from 0.1 to 0.4 for continental environments and 0.4 to 1.0 for marine environments (*Andreae and Rosenfeld*,

2008; *Pringle et al.*, 2010). However, these estimates are based on limited observations. For example, *Pringle et al.* (2010) were only able to compare modeled κ values against observations at fourteen sites, only three of which were from flight data. Similarly, *Moore et al.* (2013) identified 36 CCN closure studies, all of which took place in the Northern Hemisphere, and only seven of them from outside North America. Ongoing field measurements of aerosol composition and CCN activity are necessary to understand the variability of κ in time and space and the representation of cloud droplet formation in global models.

CHAPTER II

UNRAVELING THE DEVELOPMENT OF SUPERSATURATION UNDER DYNAMIC FLOW OPERATION OF CCN COUNTERS

2.1 Introduction

The Droplet Measurement Technologies (DMT) Continuous-Flow Streamwise Thermal Gradient Cloud Condensation Nuclei chamber (CFSTGC; *Lance et al.*, 2006; *Rose et al.*, 2008), based on the design of *Roberts and Nenes* (2005), has allowed for reliable measurements of CCN concentrations from both airborne and ground-based platforms. CCN measurements have been used to study compositional effects on droplet formation (e.g. *Padró et al.*, 2007; *Wex et al.*, 2007; *Petters and Kreidenweis*, 2007; *Petters et al.*, 2009; *Asa-Awuku et al.*, 2010; *Rose et al.*, 2010), the effects of aging and mixing state on CCN activity (e.g. *Kuwata et al.*, 2008; *Cubison et al.*, 2008; *Roberts et al.*, 2010; *Bougiatioti et al.*, 2011; *Hersey et al.*, 2013), surface activity effects on droplet formation (e.g. *Padró et al.*, 2007; *Engelhart et al.*, 2008; *Asa-Awuku et al.*, 2009; *Sareen et al.*, 2013), and droplet activation kinetics (e.g. *Engelhart et al.*, 2008; *Sorooshian et al.*, 2008; *Asa-Awuku et al.*, 2009; *Lance et al.*, 2009; *Murphy et al.*, 2009; *Bougiatioti et al.*, 2009, 2011; *Raatikainen et al.*, 2012).

Moore and Nenes (2009) introduced Scanning Flow CCN Analysis (SFCA) which allowed for the rapid measurement of CCN spectra by varying the instrument flow rate in 20–120 s cycles. The ability to quickly measure CCN spectra is advantageous for airborne measurements (*Moore et al.*, 2012; *Hersey et al.*, 2013; *Russell et al.*, 2013) as well as ground-based measurements of rapidly changing environments (*Hildebrandt Ruiz et al.*, 2015). Recently, *Raatikainen et al.* (2014) expanded the computational SFCA model and demonstrated that small pressure and flow fluctuations can have a large impact on instrument supersaturation via compression heating or expansion cooling. In this work, we use both theoretical analysis and laboratory experiments to characterize the performance of the CFSTGC under dynamic flow operation.

2.2 Methods

2.2.1 Instrument description

The DMT CFSTGC CCN Counter has been extensively characterized by *Lance et al.* (2006) and *Rose et al.* (2008). The growth chamber in the CFSTGC is a cylinder with length 50 cm and inner diameter 2.3 cm. Sample aerosol is introduced at the top of the column along the centerline encased in particle-free sheath air. A linear temperature gradient is maintained along the streamwise direction with three thermoelectric coolers on the outside of the column. Owing to the positive temperature gradient applied to the column and higher diffusivity of water vapor compared to air, a stable supersaturation is generated along the centerline of the column. This supersaturation within the instrument is a function of the temperature gradient along the column, the flow rate through the column, and the pressure of the column. Particles that activate into droplets are counted with an optical particle counter (OPC) with size range 0.75 - 10.0 μm.

Moore and Nenes (2009) demonstrated that rapid, continuous supersaturation spectra could be made with the CFSTGC by varying the flow rate in the column while maintaining constant pressure and streamwise column temperature gradient. Starting at a minimum flow rate Q_{min}, the flow rate is linearly increased to a maximum flow rate Q_{max} over a ramp time t_{up}. The flow rate is then linearly decreased back to the minimum flow rate over a ramp time t_{down}. If desired, the flow flow rates may be held constant at the minimum and maximum flow rates for hold times t_{base} and t_{peak}, respectively. If the characteristic timescale of flow change is larger than the characteristic timescale of diffusivity of momentum, heat, and mass, the instantaneous velocity, temperature, and water vapor profiles in the column approach their steady-state profiles, thus generating a quasi-steady-state supersaturation. The diffusion of momentum is the slowest transport process. At 298 K and 1013 mbar, the characteristic timescale of diffusivity of momentum is about 10 seconds (*Moore and Nenes*, 2009). Therefore, for characteristic timescales of flow change greater than 10 seconds, SFCA can provide CCN spectra with CCN concentrations corresponding to the instantaneous supersaturation in the instrument.

Up to this point, implementation of SFCA with the DMT CFSTGC has been with a

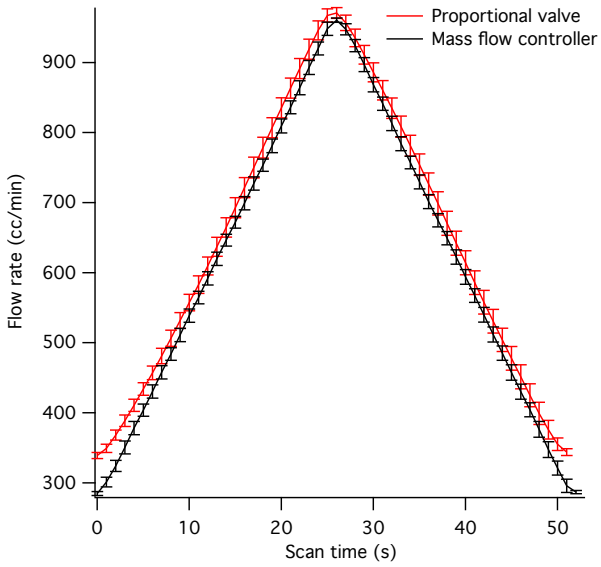

Figure 2.1: Average SFCA flow rate scan for flow rates controlled by the CFSTGC proportional valve and a mass flow controller.

software patch that allows for users to define SFCA flow cycles. The flow rate is changed by varying the voltage to the proportional valve that controls the flow rate through the instrument. The software patch allows for easy adoption of SFCA, but there are limitations in using existing hardware of the CFSTGC to operate in SFCA mode. The hysteresis in the CFSTGC proportional valve causes flow scans to be asymmetric, actual flow scan periods and flow rate ranges deviated from nominal values, and CCN concentrations would rapidly decrease to zero during the downscan portion of the flow scan.

In this work, the proportional valve is bypassed in favor of controlling the flow rate with a mass flow controller (MKS Instruments model M100B01313CR1BV). A microcontroller board (Arduino Uno) is used to send set point inputs to the mass flow controller. The combination of the mass flow controller and microcontroller allows for more precise control of instrument flow rate and more flexible implementation of the flow rate waveform. Figure 2.1 shows a comparison of average flow scans produced by the CFSTGC proportional valve and the mass flow controller. Scans with the CFSTGC proportional valve were nominally set for a flow rate range of 300-1000 cc/min over a 40 second period. The resulting scans had a flow rate range of 340-970 cc/min over a 51 second period. Scans with the mass flow controller were targeted to have a flow rate range of 300-950 cc/min over a 52 second period.

The resulting scans had a flow rate range of 285-960 cc/min over a 52 second period. The flow scans with the mass flow controller are smoother and have less variability than produced with the proportional valve in the CFSTGC. In addition to the trapezoidal and triangular waveforms allowed by the original SFCA software, the new hardware module allows for a variety of waveforms to be implemented, including, but not limited to, sinusoidal, polynomial, and sigmoidal waveforms. In this work, we will focus on triangular and sinusoidal waveforms.

2.2.2 Instrument model

2.2.2.1 Full model description.

The CFSTGC model of *Raatikainen et al.* (2014) accurately simulates instrument operation during SFCA operation. It is based on the constant flow CFSTGC model of *Raatikainen et al.* (2012) with the transient inlet boundary conditions of *Moore and Nenes* (2009). The model calculates instantaneous supersaturation, temperature, pressure, velocity, and water vapor concentration fields. Droplet sizes are calculated using a computationally efficient module that couples the water vapor and droplet phases. Necessary inputs to the model are total flow rate and sheath-to-aerosol (SAR) flow ratio; chamber pressure; column top temperature, column inner wall temperatures, and wall thermal efficiency $\eta = \frac{\Delta T_{\text{inner}}}{\Delta T_{\text{outer}}}$ calculated from instrument calibration experiments; and aerosol size distributions, hygroscopicity, and water uptake coefficient. If water vapor depletion effects are ignored, final droplet sizes and instrument supersaturation are solved directly. If water vapor depletion effects are taken into account, the instrument water vapor and droplet phases are coupled via the water vapor condensation term and iterated until supersaturation and droplet sizes converge.

2.2.2.2 Simplified model description

Under conventional constant flow operation, instrument supersaturation is varied by changing the column temperature gradient while holding the pressure and flow rate through the column constant. In addition to those three parameters, instrument supersaturation is affected by pressure fluctuations via adiabatic cooling or heating in the CFSTGC column. Rapid pressure fluctuations can affect the instrument supersaturation through adiabatic expansion or compression. This provides a heating or cooling source given by

Table 2.1: Calibration experiments performed for this work.

ΔT (K)	Pressure (mb)	Waveform	Period (s)	ΔT (K)	Pressure (mb)	Waveform	Period (s)
10	900	Triangle	30	10	600	Triangle	30
			60				60
			120				120
			30				240
		Sinusoid	30			Sinusoid	30
			60				60
			120				120
			240				240

$$\frac{dT}{dt} = \frac{\gamma - 1}{\gamma} \frac{T}{P} \frac{dP}{dt} \tag{4}$$

where γ is the heat capacity ratio of dry air and T and P are the temperature and pressure in the CFSTGC column, respectively. *Raatikainen et al.* (2014) included two types of pressure fluctuations: external pressure fluctuations at the instrument inlet, $\frac{dP_{\text{inlet}}}{dt}$, and the pressure drop from the instrument inlet to the CFSTGC column that is a function of the change in flow rate, $\frac{dQ}{dt}$. Including these pressure fluctuation terms, the supersaturation as a function of flow rate can be written as

$$s_{\text{SFCA}}(Q) = s_{\text{CF}}(Q) - \frac{\beta}{P_{inlet} T} \left(\frac{dP_{inlet}}{dt} \right) + \frac{\beta k}{P_{inlet} T} \left(\frac{dQ}{dt} \right) \tag{5}$$

where $s_{\text{CF}}(Q)$ is the supersaturation at flow rate Q during constant flow operation, β is a constant composed of thermodynamic and instrument parameters, and k is a constant that scales the pressure drop to the CFSTGC column with flow rate. The supersaturation that develops during SFCA operation can therefore be seen as the supersaturation that would develop during constant flow operation at the same flow rate plus a contribution from external pressure fluctuations and a contribution from the change in instrument flow rate.

2.2.3 Calibration experiments

A summary of the SFCA calibration experiments is given in Table 2.1. The experiments were performed in order to evaluate the effects of pressure, type of waveform, and waveform period on instrument supersaturation during SFCA operation. The type of waveform and waveform

period are both expected to have differing contributions to the SFCA supersaturation based on differing changes in flow rate for each waveform or waveform period. The experimental setup for evaluating SFCA operation follows that of *Moore and Nenes* (2009). Ammonium sulfate calibration aerosol is size-selected using a differential mobility analyzer (DMA 3080, TSI). The classified aerosol is mixed with particle-free dilution air before being split between a condensation particle counter (CPC 3010, TSI) and the CFSTGC. Pressure inside the CFSTGC is controlled with a DMT pressure control box. A critical orifice is placed upstream of the CFSTGC and the flow is split between the instrument and the pressure control box. For the 900 mb experiments, a 0.019" orifice (O'Keefe K4-19-SS) was used. For the 600 mb experiments, a 0.016" orifice (O'Keefe K4-16-SS) was used.

Concentrations of CCN from the CFSTGC and total condensation nuclei (CN) from the CPC are used to calculate the fraction of particles of size D_p, $R_a\left(D_p\right)$, that activated into cloud droplets in the CFSTGC. To find the supersaturation generated inside the CFSTGC column, $R_a\left(D_p\right)$ data are fit to the sigmoidal equation:

$$R_a\left(D_p\right) \equiv \frac{CCN}{CN} = A + \frac{B - A}{1 + \left(\frac{Q}{Q_{50}}\right)^{-C}} \tag{6}$$

where Q is the instantaneous flow rate in the CFSTGC and A, B, C, and Q_{50} are constants that describe the sigmoid's minimum, maximum, slope, and inflection point, respectively. Sigmoids were fit automatically using a Levenberg-Marquardt least-squares curve fitting routine. The Q_{50} value define a critical flow rate at which particles of a certain size in the instrument activate into cloud droplets. The supersaturation required to activate the dry ammonium sulfate particles is calculated with Köhler Theory (*Köhler*, 1936) using parameters used by *Moore and Nenes* (2009).

The resulting points are fit with a second order polynomial, defining the dependence of instrument supersaturation on instrument flow rate. The fits are extended to cover to entire flow rate range of the calibration with a constraint that the maximum and minimum supersaturation for both upscans and downscans occur at the maximum and minimum flow rates, respectively. Uncertainties in the minimum and maximum supersaturations are

estimated from the 95% confidence bands of the curve fitting.

2.3 Results

2.3.1 Calibration results

The results from the set of calibrations are shown in Figure 2.2 for triangle waves and Figure 2.3 for sinusoid waves. For comparison, calibrations at various constant flow conditions are also shown in the figures. It can be seen that some of the calibrations show large deviations from the supersaturation curve obtained from conventional operation while others behave similarly to conventional operation. In this section, we will explore the effects of varying instrument pressure, type of waveform, and waveform period on the supersaturation generated by the CFSTGC.

The effects of changing instrument pressure on instrument supersaturation range is shown in Figure 2.4. The change is calculated as the change in supersaturation range going from 900mb to 600 mb. For both triangle and sinusoid waves and for all flow scan periods, the instrument supersaturation range is reduced with lower pressure inside the CFSTGC column. With one exception, the percent change in supersaturation range is fairly consistent, between

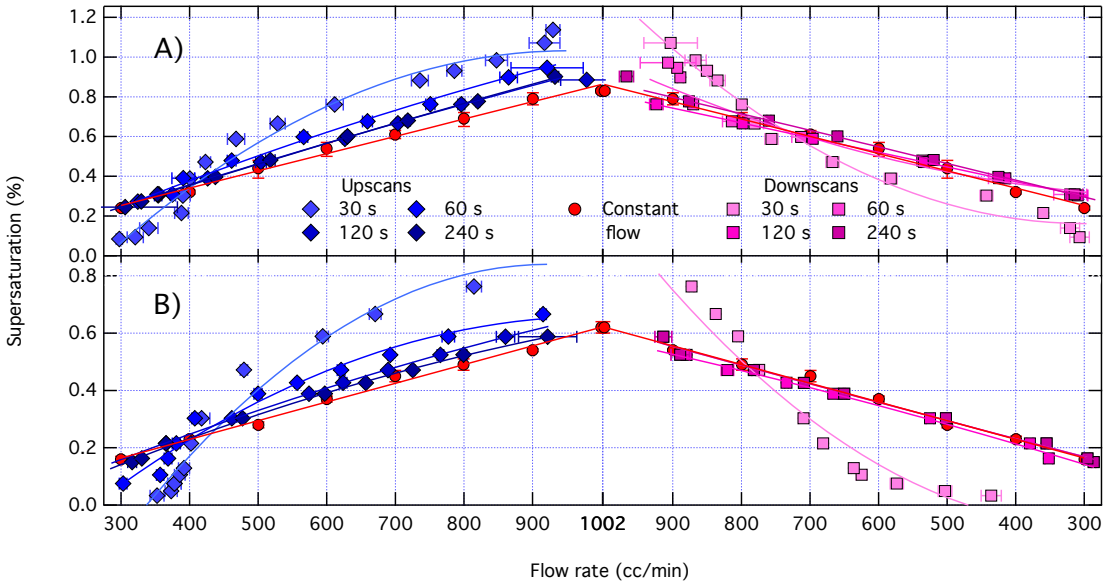

Figure 2.2: Calibration curves of instrument supersaturation versus flow rate for triangle flow scans at A) 900 mb pressure and B) 600 mb pressure. Also shown in red are instrument supersaturations at constant flow rates.

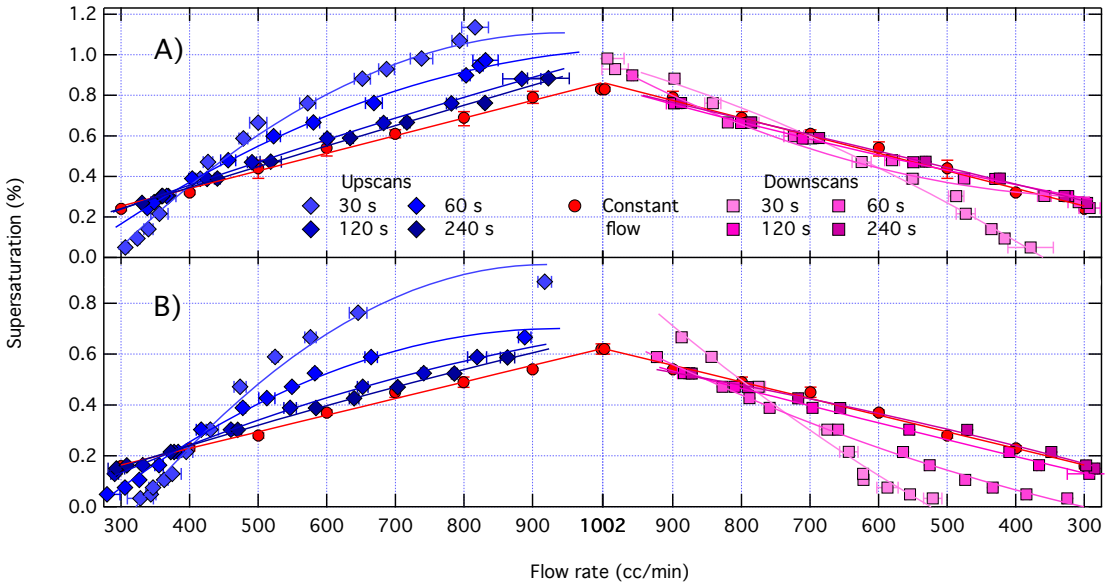

Figure 2.3: Calibration curves of instrument supersaturation versus flow rate for sinusoid flow scans at A) 900 mb pressure and B) 600 mb pressure. Also shown in red are instrument supersaturations at constant flow rates.

about 0.07 and 0.22% supersaturation units. This reduction in supersaturation with pressure is consistent with previous studies (*Roberts and Nenes*, 2005; *Moore and Nenes*, 2009).

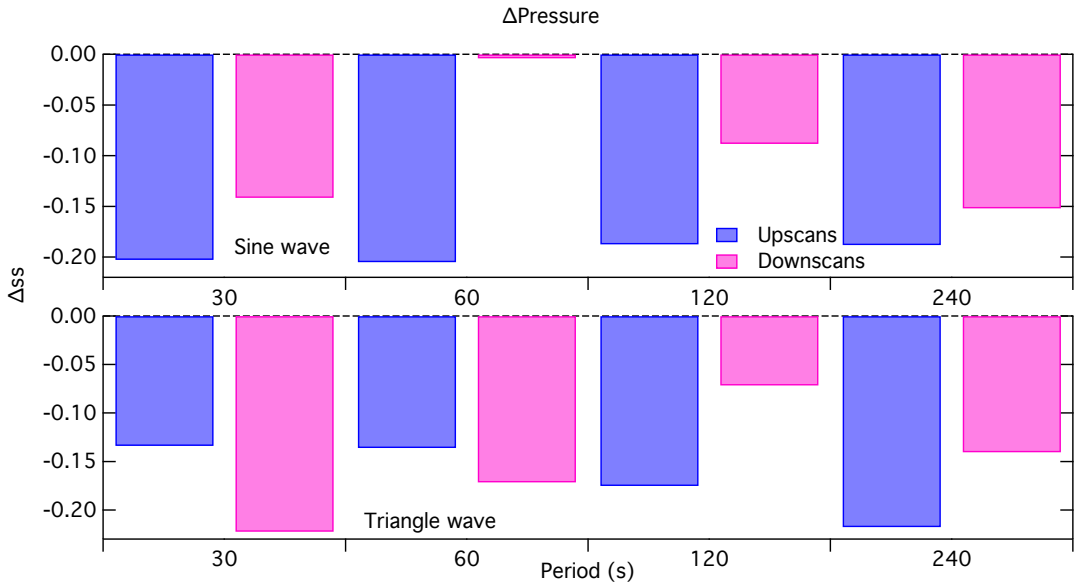

Figure 2.4: Change in instrument supersaturation going from 900 to 600 mb instrument pressure.

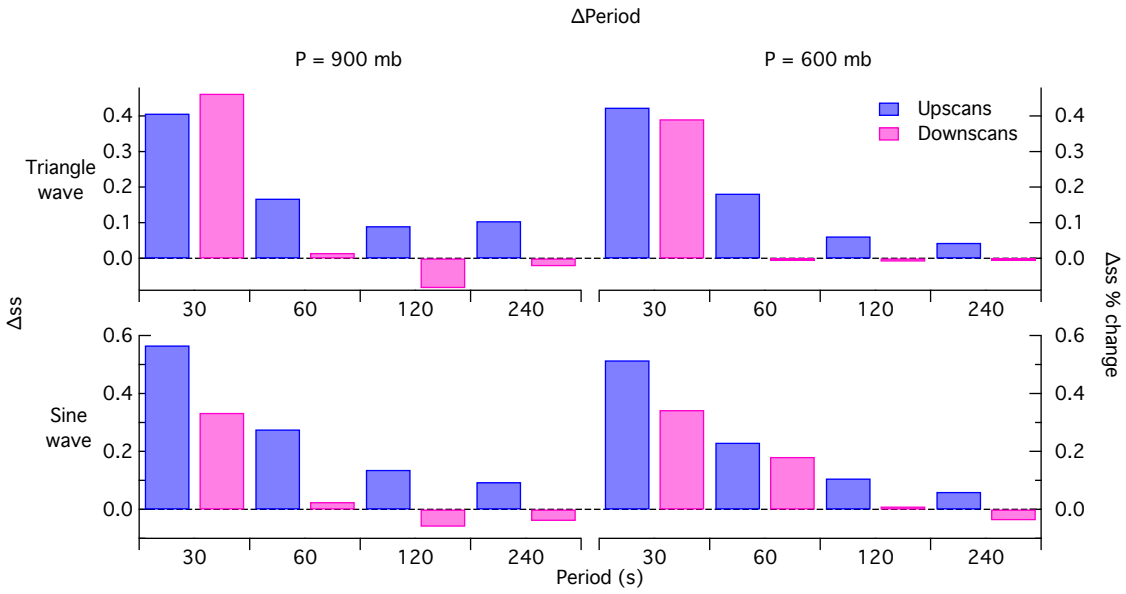

Figure 2.5: Change in instrument supersaturation relative to constant flow operation due to changing wave period.

The effects of changing flow scan period on instrument supersaturation range is shown in Figure 2.5. The change is calculated as the change in the supersaturation range during SFCA operation at a specific flow scan period compared to the base case of the supersaturation range from constant flow operation spanning the same flow rate range. For both triangle and sine waves, larger expansions of the supersaturation range are seen at shorter flow scan periods. Intuitively, this makes sense since the longer the flow scan period is, the more it starts to approximate constant flow operation. As the flow scan period decreases, the rate at which the flow rate changes increases, increasing the contribution of the flow rate change term to the supersaturation generated during SFCA operation. The larger rate of change in flow rate contributes to additional supersaturation due to greater expansion cooling during the upscans and less supersaturation due to greater compression heating during the downscans.

The effects of the flow scan waveform on instrument supersaturation range is shown in Figure 2.6. The change is calculated as the change in supersaturation range going from triangle to sinusoidal waveforms. In general, an expansion in the supersaturation range is seen going from triangle waves to sine waves. For a given waveform period with the same minimum and maximum flow rates, a sine wave will have a larger maximum absolute value of $\frac{dQ}{dt}$

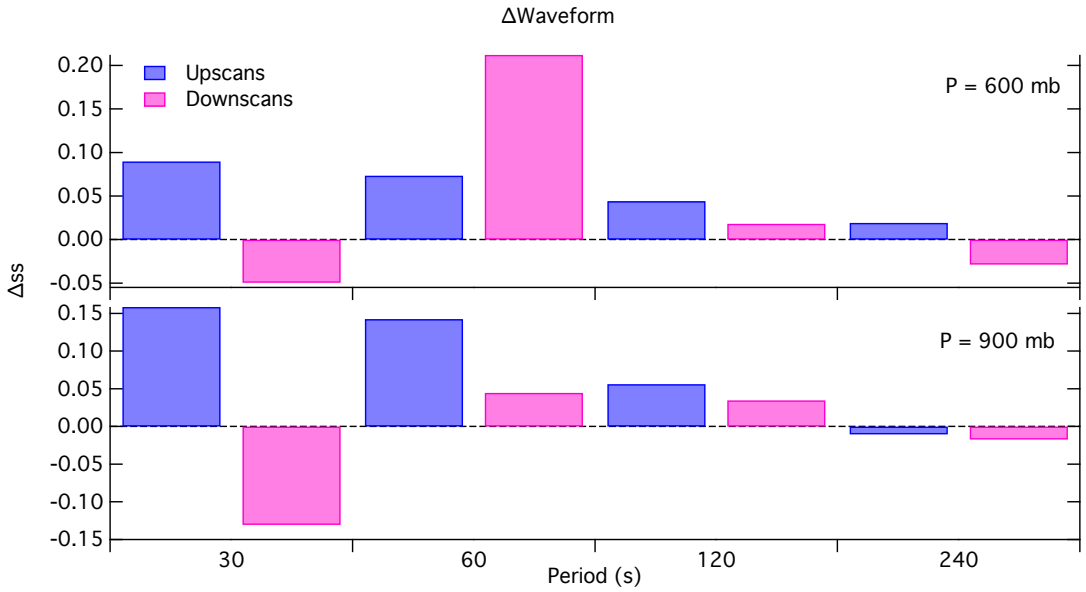

Figure 2.6: Change in instrument supersaturation going from triangle to sine waves.

than a triangle wave. Again, this larger rate of change in flow rate contributes to additional supersaturation due to expansion cooling during the upscans and less supersaturation due to compression heating during the downscans. At 240s flow scans periods, both triangle and sine waves approximate constant flow operation, and they is no large difference in supersaturation range between the two waveforms.

2.3.2 Ambient data

This section presents an evaluation of the performance of the CFSTGC operating in SFCA mode during aircraft operation using the CFSTGC model of *Raatikainen et al.* (2014). The full model is run for both calibrations and ambient data collected during flights to

Table 2.2: A summary of average instrument parameters used as inputs to the CFSTGC model.

Measurement	Date	Flow rate (cc/min)	SAR	P (mbar)	T1 (K)	η
SENEX calibration	17 June 2013	268.4–936.5	10	602.5	299.9	0.9
SENEX flight 5	13 June 2013	277.3–974.3		603.3	311.0	
SEAC^{4}RS calibration	30 July 2013	281.4–1051		450.5	309.9	
SEAC^{4}RS flight 12	27 August 2013	214.8–977.4		449.3	305.2	
DAQ-Houston calibration	27 February 2014	291.8–961.5		499.4	300.4	
DAQ-Houston flight 6	14 September 2013	214.0–959.4		499.3	307.9	

compare instrument performance on the ground during calibrations against performance during airborne sampling during research flights.

Data from three field studies–SENEX, SEAC^{4}RS, and DISCOVER-AQ Houston (DAQ-H)–are included. The SENEX (Southeast Nexus-Studying the Interactions between Natural and Anthropogenic Emissions at the Nexus of Climate Change and Air Quality) campaign took place in the southeast United States from June – July 2013. The SENEX campaign was part of a larger effort to study the summertime emission sources, chemistry, and meteorology in the southeast United States (*Warneke et al.*, 2016). Results here are shown for research flight five on 11 June 2013. The goals of this research flight was to study the Birmingham, Alabama, urban plume and nearby power plant emissions along with a fly over of the ground site at Centreville, Alabama. The SEAC^{4}RS (Studies of Emissions and Atmospheric Composition, Clouds and Climate Coupling by Regional Surveys) campaign was based in Houston, Texas from August – September 2013. Part of the goals of SEAC^{4}RS was the study the emissions and impact of forest fires in the central and western United States. Results here are shown for research flight 12 on 27 August 2013 that sampled the Rim Fire in California's central Sierra Nevada. The DISCOVER-AQ (Deriving Information on Surface conditions from Column and Vertically Resolved Observations Relevant to Air Quality) campaign was based in Houston, Texas, from August – September 2013. A series of DISCOVER-AQ campaigns were designed to study the sources and variability of near surface air pollution to address the challenges of monitoring air pollution from space. Results here are shown for research flight six on 14 September 2013.

A summary of the instrument parameters used as inputs to the CFSTGC model are shown in Table 2.2. The parameters are average values during periods in which the model was run. The sheath-to-aerosol flow ratio in the CFSTGC is a function of flow rate but has little impact on the instrument supersaturation and is assumed to be constant at ten. The wall thermal efficiency, η, is assumed to be 0.9.

Flight data time series of the total flow rate, column pressure, and column top temperature are shown in Figure 2.7. Figure 2.7 shows how instrument parameters that affect supersaturation can change in flight. In contrast, calibration experiments are typically

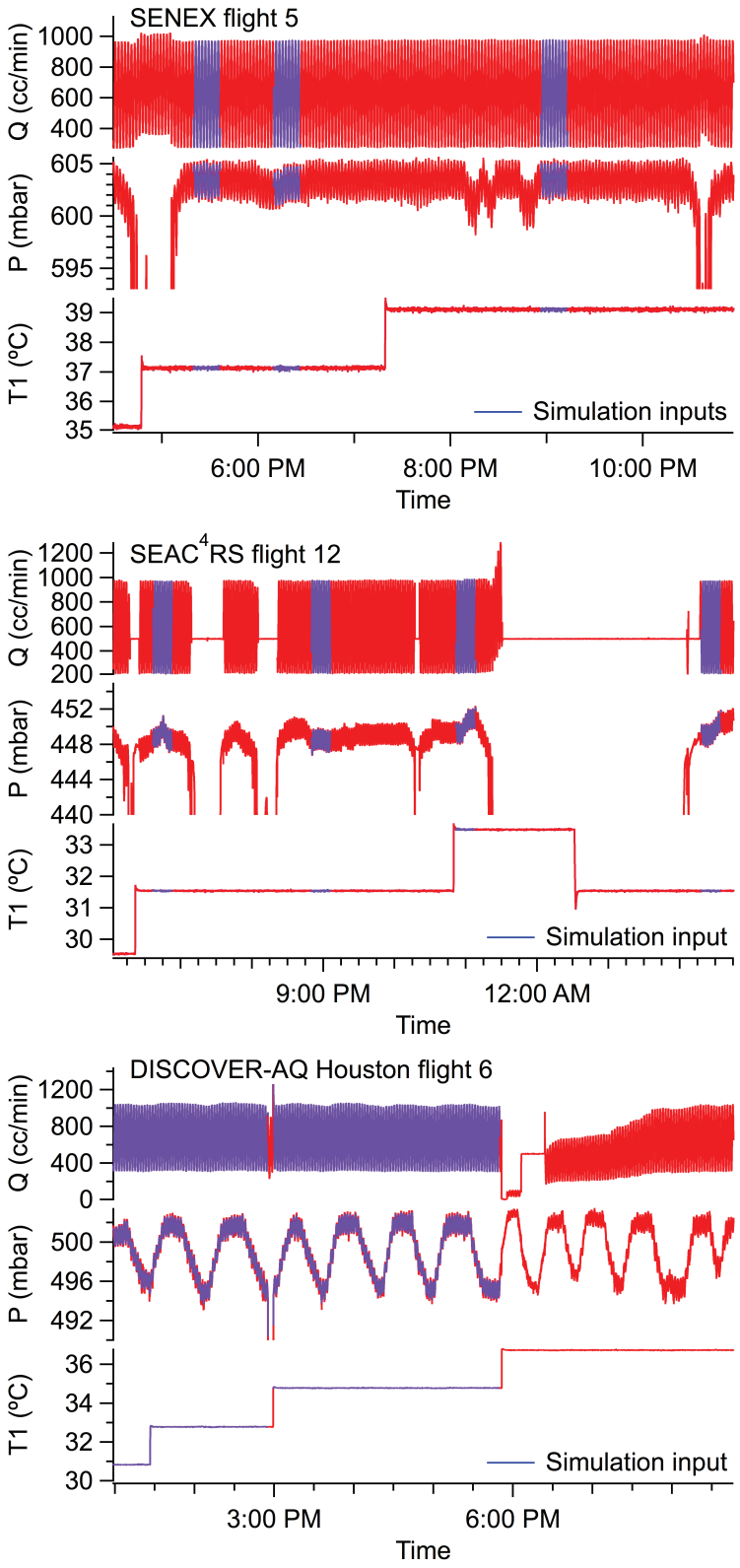

Figure 2.7: Time series of instrument parameters during airborne sampling used as inputs to calculate supersaturation with the CFSTGC model. Time periods use in the model simulations are colored in blue.

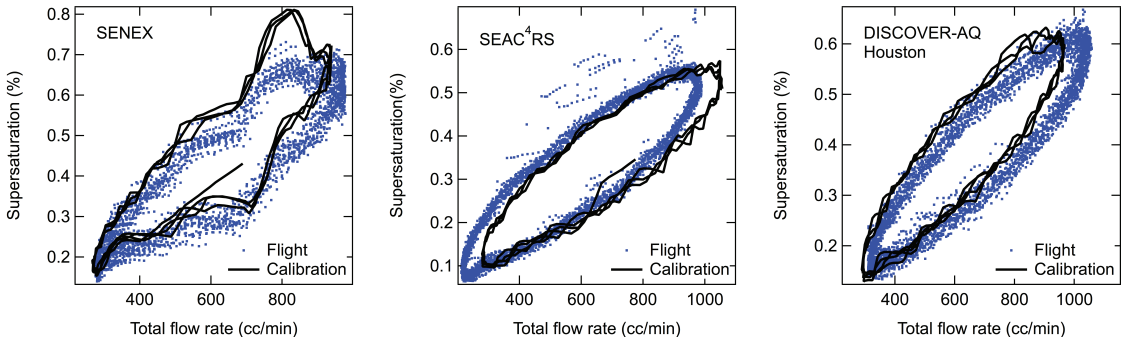

Figure 2.8: Comparison of supersaturations calculation from the CFSTGC model for calibration and flight experiments.

performed under stable operating conditions. The column top temperature, T1, changes with the temperature of the air at the inlet of the instrument. Inlet pressure is affected by changes in ambient pressure as well as the behavior of other instruments sharing the same sample line. Since the flow rate is controlled with a mass flow controller, the flow rate through the instrument will also change with changes in instrument pressure and temperature. All of these changes will affect the supersaturation in the CFSTGC in a way that may not be captured by calibration experiments.

Figure 2.8 shows the model results for instrument supersaturation during flight and calibration for each campaign. In general, the instrument supersaturations simulated for the calibrations are close to those simulated for the flights. However, the relevant instrument parameters in the CFSTGC can sometime deviate sufficiently from the calibration to change the supersaturation generated in the instrument. Figure 2.9 shows the sensitivity of the instrument supersaturation to flow rate range and column top temperature using the SEAC^{4}RS experiments. Starting with an idealized based case simulation of the flight data, two additional simulations are performed. The first is the base case with the flow rates from the calibration instead of the flow rates during the flight. The second is the base case with the flow rate and column top temperature instead of those values from the flight. Differences in the flow rate range and the column top temperature are able to explain the difference in supersaturation generated during the calibration and flight. For the experimental data simulated, most of the change in the supersaturation can be explained by differences in flow rate range with the rest explained by differences in column top temperature. For

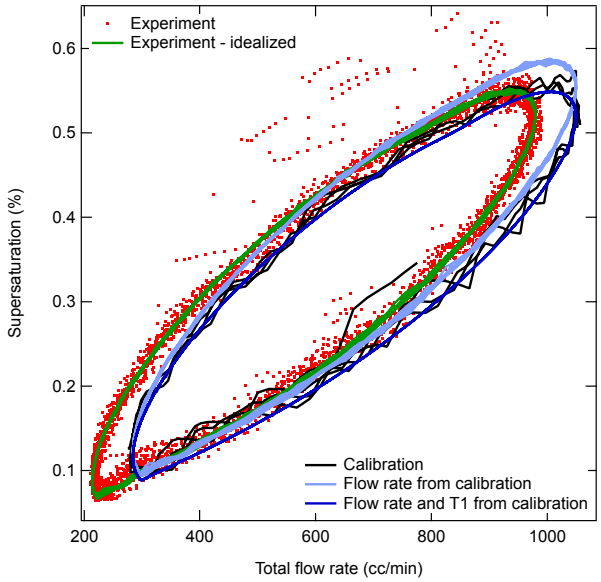

Figure 2.9: Sensitivity of modeled supersaturation on flow rate and column top temperature.

the SEAC[4]RS data, an increase in the flow rate range by 70 cc/min caused the minimum supersaturation to increase by 0.027% and the maximum supersaturation to increase by 0.036%. An increase in the column top temperature of about five Kelvin caused the minimum supersaturation to decrease by 0.0054% and the maximum supersaturation to decrease by 0.039%.

2.4 Conclusions

A module consisting of an Arduino microcontroller sending signal to a mass flow controller has been integrated with a DMT CFSTGC counter for operation in Scanning Flow CCN Analysis (SFCA) mode. The new module greatly improves the performance of SFCA with smoother flow profiles and more reliable data during downscans. The Arduino microcontroller provides a great deal of flexibility in programming a variety of flow rate waveforms.

A set of calibration experiments were performed to evaluate the effects of instrument pressure, flow scan waveform, and flow scan period on the supersaturation generated by the DMT CFSTGC during SFCA operation. Instrument supersaturation range decreases with decreasing instrument pressure while increasing with decreasing flow scan period. A change of flow scan waveform from triangle to sine wave enabled by the new hardware also brings an increase in supersaturation range.

The full CFSTGC model was run for both field and calibration experiments to compare instrument performance. The simulations show that changing conditions during flights affect instrument supersaturation in a way that cannot be captured by calibrations done on the ground. The model is able to identify the effects of multiple, small differences in instrument operational parameters on instrument supersaturation, highlighting the importance of running the model for flight experiments. In the flights data simulated in this study, the largest driver in differences in supersaturation was the flow rate range followed by the column top temperature. The effect of flow rate range on instrument supersaturation highlights the importance of controlling the flow rate in the CFSTGC. This suggests inclusion of temperature and pressure data to the mass flow controller as a method for improving flow rate control and increasing the reliability of the supersaturation generated in the instrument.

CHAPTER III

AIRBORNE AEROSOL COMPOSITION, CLOUD CONDENSATION NUCLEI, AND CLOUD DROPLET NUMBER OVER THE SOUTHEASTERN UNITED STATES DURING THE SENEX CAMPAIGN

Aerosol and cloud condensation nuclei (CCN) concentrations and aerosol size and composition data were collected in the southeastern United States aboard the NOAA WP-3D during the June–July 2013 NOAA SENEX mission, a part of the Southeast Atmosphere Study (SAS). Median size distributions in the region were bimodal with geometric mean diameter 29–32 nm and 114–135 nm. Measurements of bulk aerosol compositions show the aerosol to be up to 75% organic by volume with ammonium sulfate making up most of the remainder. The fraction of total aerosol acting as CCN ranged from 10–100% between 0.1–0.8% supersaturation. Values of the CCN-derived hygroscopicity parameter, κ, ranged from about 0.2–0.6. For critical diameters above 100 nm, κ values agree well with κ values calculated from bulk aerosol composition. With decreasing size, CCN-derived kappa values increase towards 0.6.

Aerosol composition and size distributions in the southeastern United States were also obtained from simulations with the Community Atmosphere Model (CAM) and the Community Multi-scale Air Quality Model (CMAQ). Both CAM and CMAQ fail to capture the observed aerosol size distributions, particularly the accumulation mode number. Aerosol composition from CAM produced κ values close to those derived from measured bulk composition, but CMAQ underestimates organic aerosol mass, leading to an overestimation of κ compared to measurements. The aerosol properties derived from measurements and models are used to calculate cloud droplet number using the Abdul-Razzak and Ghan droplet activation parameterization. Although measured total aerosol number was four times greater than modeled total aerosol number, the difference in resulting cloud droplet number was only a factor of about two. Cloud droplet sensitivities from the adjoint of the Abdul-Razzak and

Ghan parameterization show that differences in accumulation mode aerosol number drive most of the difference in cloud droplet number.

3.1 Introduction

The southeastern United States faces a number of conditions that makes it unique from an air quality and climate perspective. Summers in the region are warm with high humidity and intense solar insolation with frequent occurrences of air mass stagnation (*Samson and Shi*, 1988). The region is largely forested or agricultural, leading to some of the highest organic aerosol loadings in the country (*Chameides et al.*, 1988). Island cities and large point sources in rural areas contribute anthropogenic emissions that mix with biogenic emissions (*Cowling et al.*, 1998).

The southeastern United States has experienced an anomalous cooling trend with respect to the rest of the United States (*Portmann et al.*, 2009; *Goldstein et al.*, 2009) that may be explained by the interactions between biogenic and anthropogenic emissions (*Leibensperger et al.*, 2012a,b). Organic aerosol loadings in polluted air cannot be entirely explained by formation from anthropogenic precursors (*de Gouw et al.*, 2005). The uncertainty in the formation pathways of secondary organic aerosol (SOA) leads to uncertainty in its radiative forcing. Modeling work by *Hoyle et al.* (2009) found that, in the southeastern United States, the direct radiative forcing due to SOA is sensitive to the assumed partitioning of secondary organic aerosol. Previous work has suggested a role of anthropogenic emissions in the formation of organic aerosol from natural precursors (*Weber et al.*, 2007). The high amount of particle-phase liquid water associated with anthropogenic sulfate emissions may help explain why biogenic SOA in the southeastern United States is high compared to similar regions such as the Amazon (*Carlton and Turpin*, 2013). Particle-phase liquid water plays an important role in SOA formation (*Blando and Turpin*, 2000; *Ervens et al.*, 2011). Measurements of gas and particle-phase water-soluble organic carbon (WSOC) in Atlanta, GA, found that WSOC is a major component of the aerosol comprising nearly all of the SOA. The partitioning of WSOC between the gas and particle phase suggested the partitioning of semi-volatile vapors to liquid water followed by reactions in the aqueous phase to be a

dominant pathway of SOA formation in Atlanta (*Hennigan et al.*, 2009). In the eastern United States, high concentrations of particle-phase liquid water and water soluble organic matter (WSOM) relative to semi-volatile gases and organic matter lead to WSOM predominantly partitioning into liquid water. Since the presence of particle phase water is largely due to anthropogenic emissions of sulfate, this provides a pathway for anthropogenic emissions to influence the SOA produced from biogenic precursors (*Carlton and Turpin*, 2013). More recent work has provided a possible mechanism for this anthropogenically influence biogenic SOA formation (*Xu et al.*, 2015).

The region has been the subject of previous and ongoing measurement studies. The Southern Oxidants Study (SOS) was initiated in ten southern states in order to better understand and control pollution from ozone and other photochemical oxidants. In 1995 SOS undertook the Nashville/Middle Tennessee Ozone Study from 19 June to 28 July. The study included a surface chemistry network of 108 sites, five wind profiler stations, and six instrumented aircraft. The Southeastern Aerosol Research and Characterization (SEARCH) network started as part of SOS in 1992 and provides measurements of meteorological parameters, trace gases, and aerosol mass and composition (*Hidy et al.*, 2014). Other measurement networks with stations in the region include Assessment of Spatial Aerosol Composition in Atlanta (ASACA; *Butler*, 2003); Clean Air Status and Trends Network (CASTNET; *Holland et al.*, 1995); Chemical Speciation Network and Interagency Monitoring of Protected Visual Environments (CSN and IMPROVE; *Solomon et al.*, 2014); and Photochemical Assessment Monitoring Station (PAMS) (PAMS; *Chu et al.*, 1996).

The Southeastern Aerosol and Visibility Study (SEAVS) took place in the Great Smoky Mountains National Park from 15 July to 25 August 1995. The study was design to be an intensive air quality study in a rural environment. Extensive gas and particle measurements were made to characterize the mass and composition of aerosol as well as understand the contribution of individual chemical constituents to aerosol mass and extinction. Examination of aerosol polarity and functional group composition using Fourier transform infrared spectroscopy suggested that secondary formation processes have a large impact on the concentration, composition, and size of the fine aerosol in the park (*Blando et al.*, 1998). Estimates

of sub-saturated particle hygroscopicity using humidity-controlled optical particle counter size distribution measurements suggested that particle hygroscopicity could be well-explained by only assuming the sulfate species of the aerosol were hygroscopic. However, the lack of a trend in the organic aerosol contribution to particle hygroscopicity could be attributed to the sparseness of the data (*Hand et al.*, 2000).

Since the last intensive field measurement campaigns, anthropogenic emissions in the southeastern United States have begun to decline (*Hidy et al.*, 2014; *Tanner et al.*, 2015). Advances in our scientific understanding of processes in the biosphere and atmosphere along with improvements in instrumentation for laboratory and *in situ* measurements motivated another intensive field study in the southeastern United States–the Southeast Atmosphere Study (SAS)–to build upon previous studies. The Southeast Nexus (SENEX) was a airborne measurement component of SAS led by the National Oceanic and Atmospheric Administration (NOAA). Aerosol and cloud condensation nuclei (CCN) concentrations and aerosol size and composition data were collected aboard the NOAA WP-3D during the SENEX campaign. This work presents measurements of CCN activity as well as calculations of cloud droplet number from a parameterization driven input parameters measured during SENEX and derived from model simulations. Calculated droplet number sensitivities identify the parameters driving the difference between droplet number calculated from measurements and modeled parameters describing the aerosol size and composition.

3.2 Methods

3.2.1 SENEX overview

Measurements were made aboard the National Oceanic and Atmospheric Administration (NOAA) WP-3D aircraft based in Smyrna, Tennessee (36°00′32″N, 86°31′12″W). Twenty research flights were conducted between 27 May and 10 July 2013. Descriptions of the research flight are given in Table 3.1. Research flight tracks are shown in Figure 3.1.

Table 3.1: Research flights during 2013 SENEX.

	Date	Local Time (CDT, UTC-5 hrs.)[a]	Flight Location and Description	Emission sources
1	29 May	16:58-19:39	Jacksonville, FL; St Johns River	biogenic/urban; power plant
2	31 May	10:11-12:30	Jacksonville, FL; St Johns	biogenic/urban; power plant
3	3 June	10:14-15:19	Birmingham, AL; EC Gaston, Johnsonville, Cumberland, Colbert; Centreville, AL, spiral	urban; power plant; biogenic
4	10 June	09:55-16:30	Haynesville Shale	shale play
5	11 June	11:30-17:57	Centreville and Birmingham, AL; EC Gaston	biogenic/urban; power plant
6	12 June	09:48-15:31	Atlanta, GA; Scherer, Bowen, Yates, Wansley, Harlee Branch	urban; power plant
7	16 June	10:16-16:49	Atlanta, GA; Scherer, Bowen, Yates, Wansley, Harlee Branch; paper mills, landfills, poultry farming	urban; power plant; point sources/agricultural
8	18 June	16:53-19:17	Aborted flight; Franklin, TN	
9	19 June	17:30-23:29	Atlanta, GA	urban
10	22 June	10:01-17:09	Birmingham and Centreville, AL; Atlanta, GA; EC Gaston; coal mines, land fills, paper mills	urban/biogenic; power plant; point sources
11	23 June	10:08-17:22	Indianapolis, IN; biogenic/landscape emission change; Johnsonville, Cumberland	urban; biogenic; power plant
12	25 June	10:18-17:25	Haynesville Shale	shale play
13	26 June	09:57-15:37	Fayetteville Shale; Ozarks; Independence	shale play; biogenic; power plant
14	29 June	10:26-22:39	Centreville, AL; C-130 intercomparison; Birmingham, AL; James H Miller Jr, EC Gaston	biogenic; urban; power plant
15	2 July	20:08-02:51	Birmingham and Centreville, AL; JH Miller, EC Gaston, Gorgas, US Steel, Greene County	urban/biogenic; power plant
16	3 July	19:56-02:55	New Madrid, White Bluff; agricultural fire	power plant; biomass burning
17	5 July	09:52-16:24	Ozarks; St. Louis, MO; Archer Daniels Midland biofuel refinery	biogenic; urban; point source
18	6 July	09:19-16:18	Marcellus Shale	shale play
19	8 July	10:11-16:44	Fayeteville Shale; New Madrid	shale play; power plant
20	10 July	08:53-15:49	coal mines, paper mill, hog farming	point source/agricultural

[a] Research flights 1-2 were EDT, UTC-4 hrs. Research flight 3 originated EDT and landed CDT. Research flight 20 originated CDT and landed EDT.

3.2.2 Measurements

3.2.2.1 Aerosol size distribution

Particle number concentration as a function of dry size from 4–7000 nm was measured using three instruments. The nucleation-mode aerosol size spectrometer (NMASS) measures particles with dry diameters 4–70 μm (*Brock et al.*, 2000). The NMASS uses five condensation particle counters (CPCs) operated in parallel, each operating at a different temperature and with a different detection diameter. Particles of dry diameter 4, 8, 15, 30, and 55 nm are nucleated and counted independently, creating an ultrafine particle size distribution. A ultra-high sensitivity aerosol spectrometer (UHSAS) measures particles with dry diameters 70–1000 nm (*Brock et al.*, 2011). Particles enter a resonant cavity and are sized by measuring the amount of side-scattering from a 1053 nm laser. A custom-built white-light optical particle counter (WLOPC) measures particles with dry diameters 700–7000 μm. The WLOPC detects light scattered by single particles from a 3 W white light emitting diode (LED).

3.2.2.2 Aerosol chemical composition

Non-refractory, submicron aerosol chemical composition was measured with a semi-custom Compact Time-of-Flight Aerosol Mass Spectrometer (C-ToF-AMS) (*Jayne et al.*, 2000; *Jimenez*, 2003; *Allan et al.*, 2004; *Canagaratna et al.*, 2007). Particles entering the instrument are focused and impacted on a 600° C inverted-cone porous-tungsten vaporizer. The volatilized

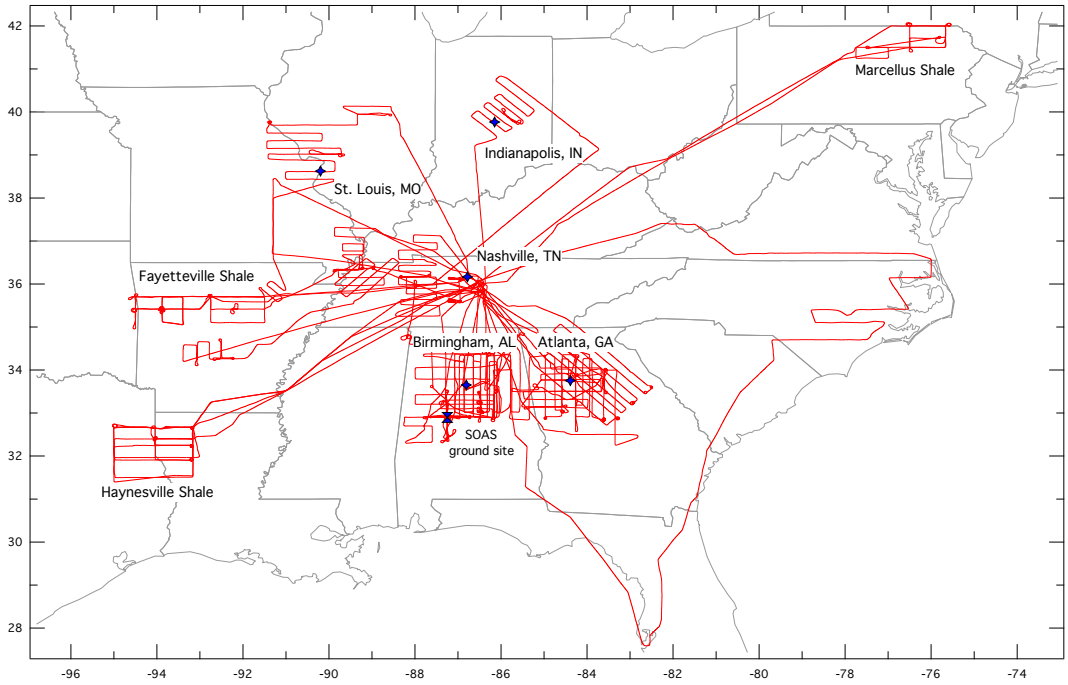

Figure 3.1: Flight tracks for the NOAA WP-3D during SENEX.

vapors are analyzed by electron ionization mass spectrometry giving mass loadings of sulfate, nitrate, ammonium, chloride, and organic aerosol constituents. Particles between 100 and 700 nm vacuum aerodynamic diameter are sampled with 100% efficiency by the C-ToF-AMS.

Single particle black carbon size, mass, and mixing state are measured with a single-particle soot photometer (*Schwarz et al.*, 2008, 2010). Particles in the instrument are passed singly through a 1 MW, 1.064 μm diode-pumped Nd:YAG laser. Particles containing black carbon are heated to vaporization by the laser, emitting black-body radiation according to the particle's black carbon mass. The particles are optically sized by detecting scattered laser light. Particles are also optically sized before entering the laser beam, allowing for the quantification of non-black carbon associated with black carbon containing particles.

3.2.2.3 Cloud condensation nuclei

Number concentration of cloud condensation nuclei (CCN) as a function of supersaturation was measured using a Continuous Flow Streamwise Thermal Gradient CCN chamber (CF-STGC) (*Roberts and Nenes*, 2005; *Lance et al.*, 2006; *Rose et al.*, 2008) in Scanning Flow

CCN Analysis (SFCA) mode (*Moore and Nenes*, 2009). The chamber in which CCN are grown is a metal cylinder 0.5 m in length with a 23 mm inner diameter. The walls and the cylinder are wetted and a positive temperature gradient is applied in the streamwise direction. Since the diffusivity of water is greater than that of heat, water vapor from the wall reaches the centerline of the growth chamber before the heat, generating a supersaturation. Particles are introduced at the top of the column along the centerline. Particles that activate and form cloud droplets are counted and sized by optical particle counter (OPC) using a 50 mW, 658 nm laser diode light source.

In SFCA mode, supersaturation in the CFSTGC is varied by cycling the flow rate through the instrument while holding the instrument pressure and applied streamwise temperature gradient of the growth chamber constant. For flow cycles slower than 10 s, the characteristic timescale of flow rate change is greater than the characteristic timescale of diffusion of momentum, and a quasi-steady-state supersaturation is generated in the instrument. In this work, the flow rate in the CFSTGC was controlled with a mass flow controller (MKS Instruments model M100B01313CR1BV) with signal to the mass flow controller generated with an Arduino Uno microcontroller board (Lin et al., in preparation). Instrument supersaturation is calibrated with ammonium sulfate aerosol according to the procedure outlined by *Moore and Nenes* (2009). During SENEX, CCN spectra were obtained every 60 s over a supersaturation range of 0.1–0.8%.

3.2.2.4 Aircraft position and meteorology

The NOAA Aircraft Operations Center (AOC) equips the WP-3D with a suite of instruments to provide information on aircraft position and motion as well as a large set of meteorological parameters. This work utilizes aircraft global positioning system (GPS) latitude, longitude, and altitude as well as updraft velocity derived from radome flow angle sensors.

3.2.3 Modeling

3.2.3.1 Cloud droplet parameterization and adjoint sensitivity

The activation of aerosol particles into cloud droplets is a dynamic process between the availability of water vapor provided by cloud-scale vertical motions and the sink of water

vapor onto CCN. Two steps are involved in calculating the number of cloud droplets that activate from a given aerosol population. First, the CCN spectrum must be computed. The CCN spectrum is the cumulative number of particles that activate into cloud droplets at a given supersaturation. Second, the maximum supersaturation that develops in a rising air parcel with updraft velocity, w, is computed. The AG00 droplet activation parameterization (*Abdul-Razzak and Ghan*, 2000) is a physically-based activation scheme commonly used in climate models. AG00 computes maximum supersaturation, s_{max}, and droplet number, N_d, explicitly as a function of updraft velocity w; aerosol chemical composition represented by the κ parameter (*Petters and Kreidenweis*, 2007); and aerosol size distribution parameters for each aerosol mode: number concentration N_a, mode diameter d_g, and geometric standard deviation σ_g.

Morales Betancourt and Nenes (2014) derived analytic expressions for the derivatives of N_d to a set of specific input parameters χ_j. This allows for the quantification of the cloud droplet number sensitivity, $\frac{\partial N_d}{\partial \chi_j}$, at the model state of N_d to ten input parameters–vertical velocity, w, and for each of the three aerosol modes, aerosol number concentration, N_{a_i}, mode diameter d_{g_i}, and hygroscopicity κ_{a_i}.

3.2.3.2 Community Atmosphere Model

The Community Atmosphere Model version 5.1 (CAM5.1) is the atmospheric general circulation model for the Community Earth System Model (CESM1.0), described in full at http://www.cesm.ucar.edu/model/cesm1.0/cam/. For the simulations in this work, the three-mode version of the modal aerosol module (MAM3; *Liu et al.*, 2012) calculates the physical properties of the aerosol. These properties are summarized in Table 3.2. Eight species–sulfate, ammonium, nitrate, primary organic matter (POM), secondary organic aerosol (SOA), black carbon, sea salt, and dust–are partitioned into three internally mixed log-normally distributed modes–Aitken, accumulation, and coarse. The geometric standard deviation of each mode, σ_{g_i}, is prescribed, but aerosol number concentration, N_{a_i}, and mode diameter, d_{g_i}, are allowed to vary in order to add up to the corresponding mass.

The CAM5.1 simulation for this work (*Morales Betancourt and Nenes*, 2014) used

Table 3.2: Aerosol parameters calculated by MAM3 for use as inputs for calculating cloud droplet number (*Liu et al.*, 2012; *Morales Betancourt and Nenes*, 2014).

Aerosol mode	Aerosol species	κ	Density (g cm^{-3})	σ_{g_i}	d_{g_i} (nm)
Aitken	Sea salt	1.160	1.90	1.6	8.7–52
	SOA	0.14	1.00		
	Sulfate	0.507	1.77		
Accumulation	Black carbon	10^{-10}	1.70	1.6	53–440
	Dust	0.068	2.60		
	POM	0.10	1.00		
	Sea salt	1.160	1.90		
	SOA	0.14	1.00		
	Sulfate	0.507	1.77		
Coarse	Dust	0.068	2.60	1.8	1000–4000
	Sea salt	1.160	1.90		
	Sulfate	0.507	1.77		

greenhouse gases concentrations and climatological sea surface temperatures corresponding to the year 2000. Emissions of aerosols, aerosol precursors, and atmospheric oxidants were set using the *Lamarque et al.* (2010) inventory, also corresponding to the year 2000. The model was run for six simulation years, and daily outputs from the final year of the simulation were used to produce a monthly average for the month of June.

3.2.3.3 Community Multi-scale Air Quality Model

The Community Multi-scale Air Quality (CMAQ) is a suite of programs developed by the United States Environmental Protection Agency (EPA) for conducting air quality model simulations, described in full at https://www.cmascenter.org/cmaq/. CMAQ is a three-dimensional, Eulerian, atmospheric chemistry and transport model that simulates the processes atmospherically relevant compounds undergo such as emission, diffusion, chemical reactions, and deposition. Aerosols in CMAQ are split between fine and coarse particles. Fine particles include the Aitken and accumulation modes which are represented by a bimodal lognormal distribution with variable standard deviations. The size distribution of fine particles evolves according to coagulation between particles, condensational growth from the vapor phase, new particle formation, transport of particles, or emission of new particles. Coarse particles are represented by a unimodal lognormal distribution with a prescribed

Table 3.3: Distribution, density, and hygroscopicity of aerosol species in CMAQ. Hygroscopicities from *Yu et al.* (2014) unless otherwise noted.

Aitken			Accumulation			Coarse		
Species	Density (g cm^{-3})	κ	Species	Density (g cm^{-3})	κ	Species	Density (g cm^{-3})	κ
Ammonium	1.8	0.5	Ammonium	1.8	0.5	Ammonium	1.8	0.5
Nitrate	1.8	0.5	Nitrate	1.8	0.5	Nitrate	1.8	0.5
Sulfate	1.8	0.5	Sulfate	1.8	0.5	Sulfate	1.8	0.5
Sodium	2.2	1.16	Sodium	2.2	1.16	Chloride	2.2	1.16
Chloride	2.2	1.16	Chloride	2.2	1.16	Sea salt	2.2	1.16
Non-carbon organic mass	2.0	0.14	Non-carbon organic mass	2.0	0.14	Primary un-speciated coarse PM	2.2	0.03
Elemental carbon	2.2	10^{-6}	SOA[a]	2.0	0.14	Soil	2.6	0.03
Primary organic carbon	2.2	0.14	Organic carbon	2.0	0.5			
			Elemental carbon	2.2	10^{-6}			
Other	2.2	0.1	Primary organic carbon	2.2	0.14			
			Trace metals[b]	2.0	0.068[c]			
			Other	2.2	0.1			

[a] SOA includes products from the oxidation of alkanes, benzene, isoprene, sesquiterpenes, terpenes, toluene, xylene, and unknown sources.
[b] Trace metals include aluminum, calcium, iron, magnesium, manganese, potassium, silicon, and titanium.
[c] Trace metals are assumed to have the same hygroscopicity as dust found in *Liu et al.* (2012).

standard deviation of 2.2 (*Binkowski*, 2003; *Byun and Schere*, 2006). The physical and chemical characteristics of aerosol species in CMAQ along with their distribution into each mode are summarized in Figure 3.3.

The CMAQ simulation for this work was carried out on a 36 km × 36 km resolution grid over the continental United States. Meteorological data were obtained offline from the Weather Research Forecasting (WRF) model and converted to CMAQ inputs using the Meteorology-Chemistry Interface Processor (MCIP). Biogenic emissions were calculated online using the Biogenic Emission Inventory System (BEIS). The simulations included extended isoprene chemistry (*Pye et al.*, 2013) that includes formation of isoprene OA from the reactive uptake of isoprene epoxides into the aqueous aerosol phase. The simulation was carried out for the entire SOAS sampling period from 28 May–18 July with an additional five days beforehand for spin-up.

3.3 Results

Results have been averaged spatially to the CAM and CMAQ grid cells shown in Figure 3.2. Four CAM grid cells–CAM NE, CAM NW, CAM SE, and CAM SW– and one CMAQ grid cells are considered. Aircraft data for this analysis are restricted to pressure levels greater than 900 mb, corresponding to about the lowest 1 km of the atmosphere. Over the course

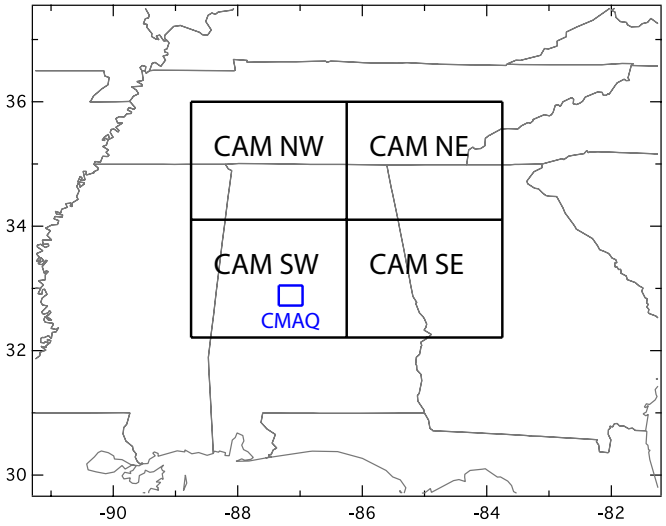

Figure 3.2: Model grid cells used in the work. Shown are four grid cells from CAM–referred to as CAM NE, CAM NW, CAM SE, and CAM SW–and the CMAQ grid cell containing the SOAS ground site.

of SENEX, the WP-3D flew between 900–970 mb pressure when sampling in the areas of interest. The WP-3D was primarily sampling in the boundary layer during this period with water vapor measured by the WP-3D being greater than 10 g kg^{-1} for 96% of the data. Outputs from the models have been averaged vertically to roughly correspond to the same vertical section of the atmosphere as the aircraft data. For CAM, this corresponds to the third through fifth model layers. For CMAQ, it corresponds to the fifth through seventh model layers.

3.3.1 Particle size distributions

Average particle size distributions are shown in Figure 3.3. The measured size distributions are obtained by computing the median and interquartile range for in each size bin for all the aerosol size distribution measurements. Model output size distributions plotted are a daily average for the month of July for CAM and for the SOAS study period of 28 May–18 July for CMAQ. All the median size distributions are bimodal with a nucleation mode centered at 29–32 nm and an accumulation mode centered at 114–135 nm. No significant number of coarse mode aerosol was measured. The median size distributions contain less than one particle per cubic centimeter of aerosol greater than one micrometer.

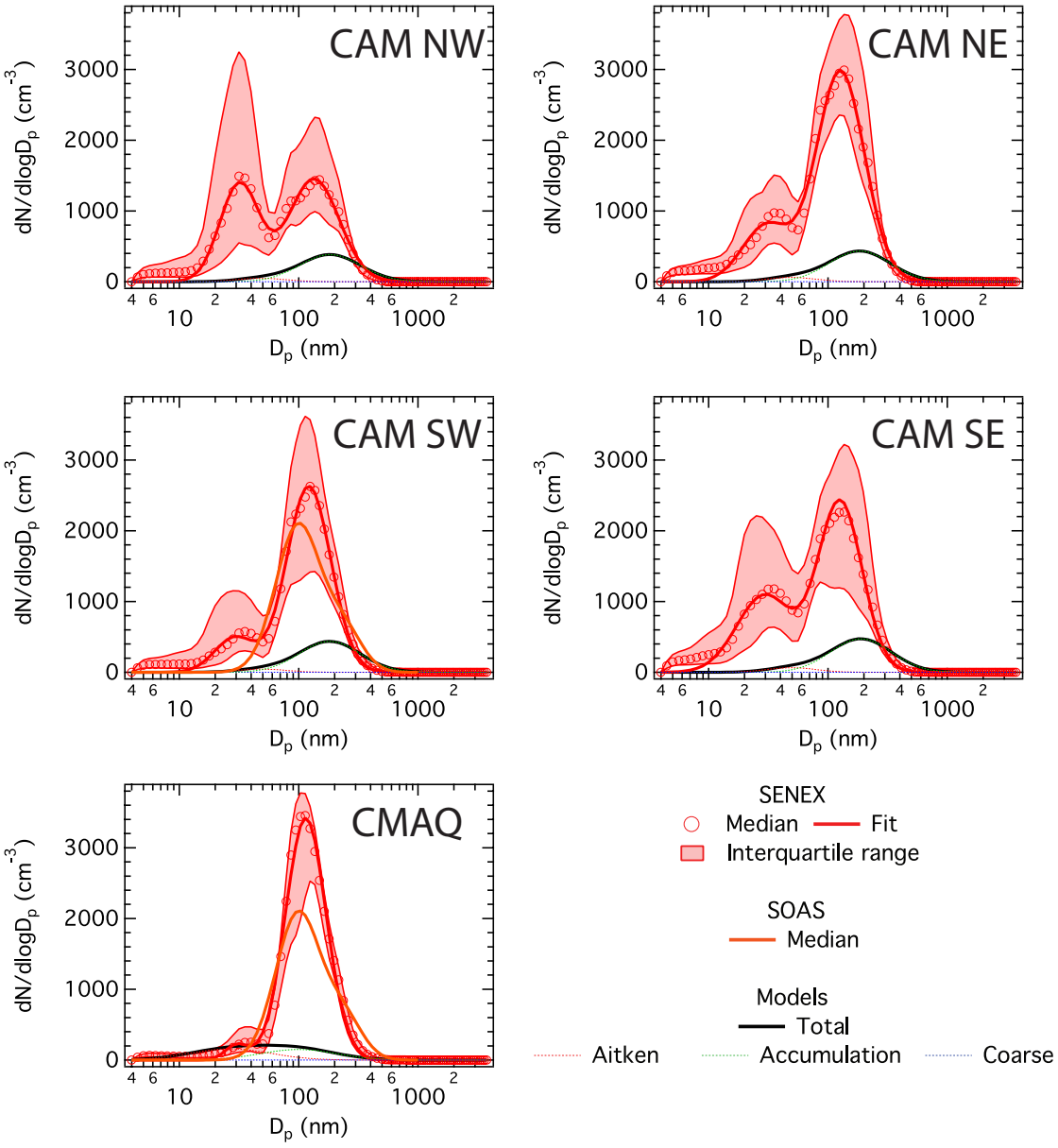

Figure 3.3: Size distributions measured aboard the NOAA WP-3D and calculated by CAM and CMAQ. Measured median size distributions are fit with two mode log-normal distributions. Shown for comparison in the CMAQ grid cell plot is the median size distribution measured during SOAS by *Nguyen et al.* (2014).

Both models fail to capture key properties of the measured size distributions, most noticeably the total number concentration. Although there is large difference between the modeled and measured size distributions, the total aerosol mass produced by CAM calculated using the size distributions and prescribed species densities is actually within about 20% of the measured aerosol mass in each CAM grid cell. The CMAQ size distribution is missing significant aerosol number in the accumulation mode, contributing to a significant underestimation to the total aerosol number as well as the total aerosol mass. Average aerosol mass measured by the C-ToF-AMS in the CMAQ grid cell was 10.88 μg m^{-3} while total aerosol mass calculated by CMAQ was 3.93 μg m^{-3}.

In Figure 3.3, the median size distribution measured by *Nguyen et al.* (2014) during SOAS is also shown in the CAM SW and CMAQ grid cells. The SOAS averaged dry size distribution was bimodal with mode diameters of 99 and 220 nm. The measured size distributions were characteristic of remote continental aerosol with no strong diurnal trend in dry aerosol volume (*Nguyen et al.*, 2014). While the accumulation mode aerosol measured during SOAS is comparable with that measured during SENEX aboard the WP-3D, no small particle events were observed during SOAS in contrast to the distinct nucleation mode aerosol observed during SENEX.

3.3.2 Particle composition

Average particle compositions are shown in Figure 3.4. Measured particle compositions are averaged from mass loadings measured by the C-ToF-AMS and SP2. The calculation of average volume fractions from mass loadings follows that of *Moore et al.* (2012). Standard inorganic species densities are used while an organic density of 1.4 g cm^{-3} (*Lance et al.*, 2009) and a black carbon density of 2 g cm^{-3} (*Schwarz et al.*, 2010) are assumed. Organics dominate the measured aerosol composition and are two-thirds to up to three-quarters of the aerosol volume. Most of the rest of the aerosol volume is ammonium sulfate, ranging from 21–27%. In the NW and SW CAM grid cells, a small amount, 3–4%, of the aerosol is ammonium bisulfate, which results from insufficient ammonium to completely neutralize the sulfate. Ammonium nitrate and black carbon are a consistent 3% and 1% by volume,

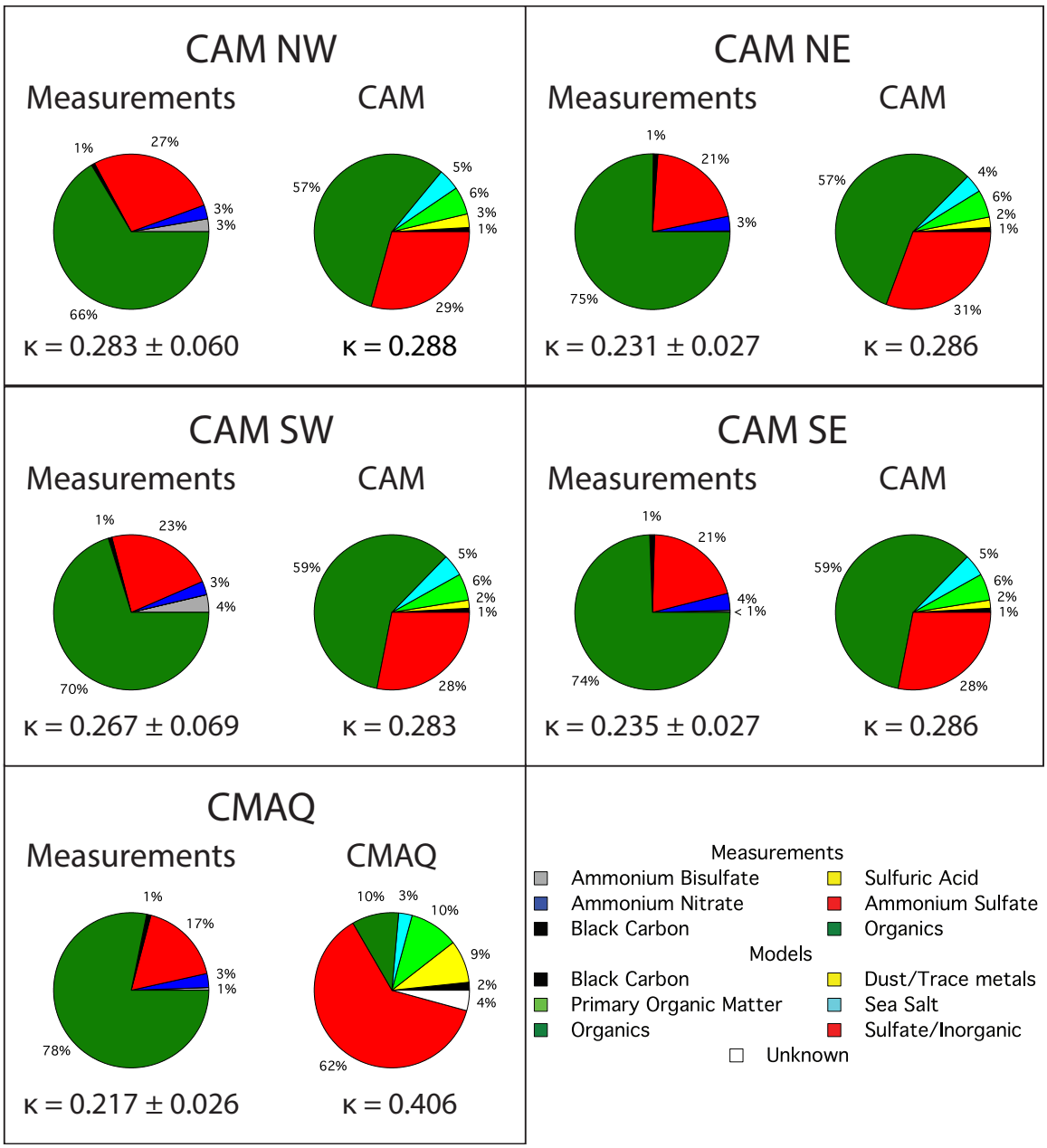

Figure 3.4: Aerosol composition measured aboard the NOAA WP-3D and calculated by CAM and CMAQ.

respectively. In the CMAQ grid cell over the SOAS ground site, organics dominate the aerosol even more, reflecting the rural location of the site. Measurements during SOAS show similar aerosol composition on the ground. *Xu et al.* (2015) found non-refractory PM_1 mass to be dominated by organics and sulfate, with mass fraction 67% and 26%, respectively.

Modeled particle compositions are daily averages for the month of July for CAM and for the SOAS study period of 28 May–18 July for CMAQ. Included in the modeled particle compositions are non-refractory species such as dust and sea salt that are measured by neither the C-ToF-AMS nor the SP2. In general, the particle compositions computed by CAM are similar to those measured aboard the WP-3D. Organics similarly dominate the aerosol composition, composing 63–65% of the volume with most of the rest made up of inorganic sulfate aerosol at 28–31%. Non-refractory aerosol volume not measured by instrument aboard the aircraft make up 6–8% of the aerosol volume. On the other hand, the CMAQ particle composition is dominated by inorganic aerosol, composing just over half of the aerosol volume with organic aerosol species composing only 30% of the aerosol. Black carbon is 2% and non-refractory species not measured by the C-ToF-AMS, dust and sea salt, is 9%. Eight percent of the aerosol is classified by CMAQ as being unknown.

The relationship between particle dry diameter and CCN activity as predicted by Köhler theory can be represented using the hygroscopicity parameter, κ (*Petters and Kreidenweis*, 2007). Bulk κ values by computing the sum of the volume weighted κ values of the constituent species. For the measured compositions, inorganic κ values are taken from *Petters and Kreidenweis* (2007), κ for organics is assumed to be 0.11 (*Cerully et al.*, 2015), and black carbon was assumed to be non-hygroscopic. For the modeled compositions from CAM, κ values *Liu et al.* (2012) are used. For the modeled compositions from CMAQ, κ values from *Yu et al.* (2014) are used, except for the trace metals, which are assumed to have the κ of dust from *Liu et al.* (2012). The bulk hygroscopicities calculated from CAM aerosol composition are within 25% for all grid cells. On the other hand, the bulk hygroscopicity calculated from CMAQ aerosol composition overestimates the measured bulk hygroscopicity due to its overestimation of inorganic species in the aerosol.

3.3.3 CCN spectra

Averaged CCN spectra are shown in Figure 3.5. The spectra are plotted as the fraction of particles that act as CCN as a function of supersaturation. This CCN activation ratio is calculated by normalizing the CCN number concentration to total fine aerosol number. The activation ratios were segregated into 15 bins from 0.1–0.8% supersaturation each with bin width 0.05%. The averaged CCN spectra are constructed by calculating the median and interquartile range of CCN number concentration and CFSTGC supersaturation in each bin. Regionally, the CCN spectra are quite consistent. Maximum CCN activation ratios of about 80–90% are observed starting at around 0.60% supersaturation. Variability in the CCN activation ratio is due to the sampling of point sources. It is especially pronounced in the SE CAM grid cell, where point sources and strong anthropogenic emissions from Atlanta contribute to high variability. In the CMAQ grid cell, there is very little variability in the CCN activation ratio, perhaps reflecting the fact the WP-3D flew over the SOAS ground site during similar times of day. Also shown in Figure 3.5 is the average CCN spectrum measured at the SOAS ground site. In the CAM SW grid cell, there is good agreement between the ground and aircraft data. In general, good agreement is seen between the ground and aircraft data. In the CMAQ grid cell, however, the agreement is not as good. This is possibly due to the relatively limited amount of sampling by the aircraft in the CMAQ grid cell. The total sampling time within the CMAQ grid cell at atmospheric pressures greater than 900 mb was only 190 minutes, with all but five minutes of it occurring during the afternoon local time. Differences in the observed size distribution may also contribute to the differences between the CCN spectra.

3.3.4 CCN-derived aerosol hygroscopicity

In the κ-Köhler framework, the critical supersaturation necessary for a particle to act as a CCN is given by

$$s_c = \sqrt{\frac{4}{\kappa d_{p,c}^3}\left(\frac{4\sigma_w M_w}{3RT\rho_w}\right)^3} \tag{7}$$

where R is the universal gas constant, T is the temperature, M_w, ρ_w, and σ_w are the molar

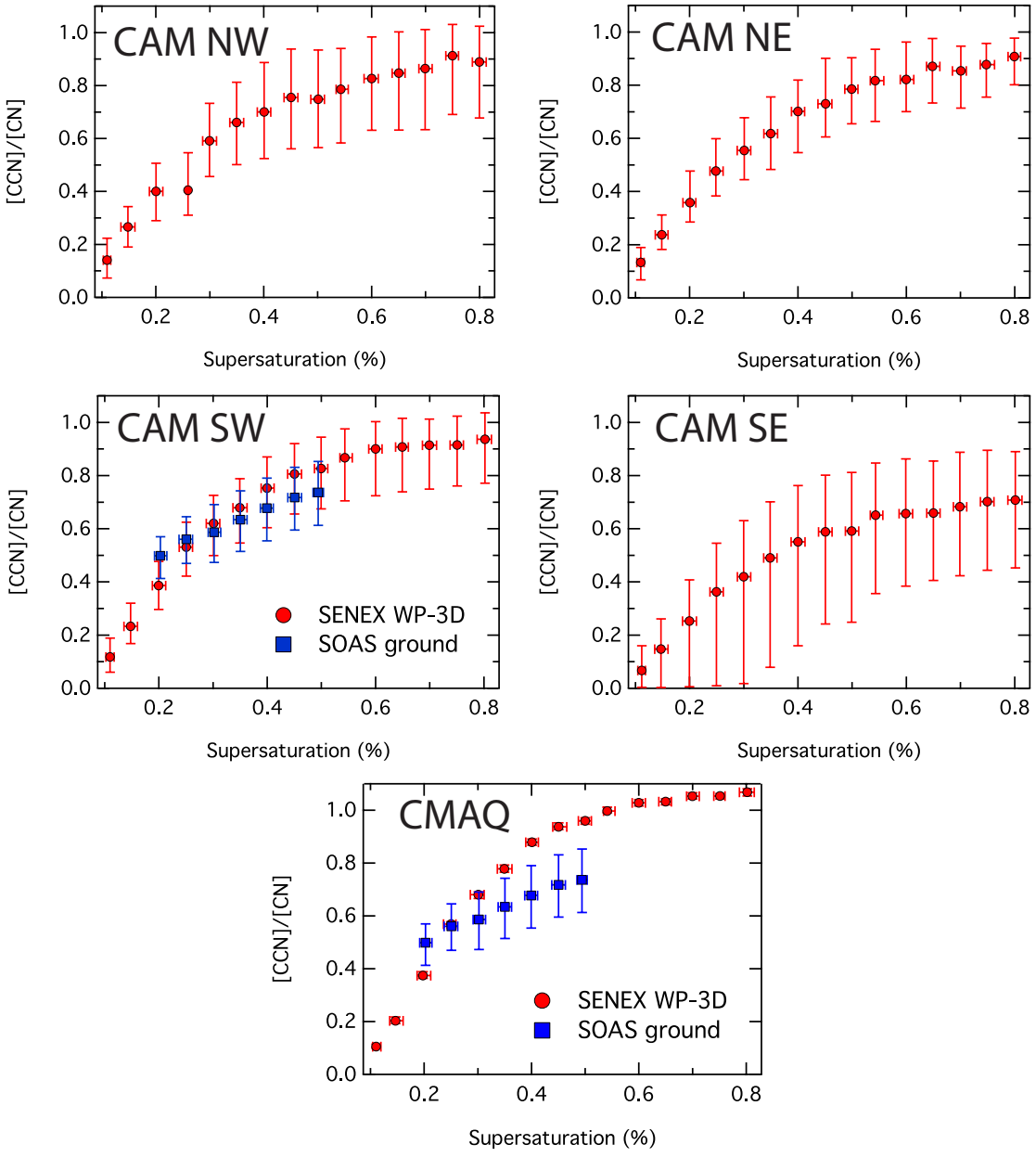

Figure 3.5: CCN activation ratio spectra measured aboard the WP-3D with CCN activation ratio spectra measured during SOAS shown for comparison.

mass, density, and surface tension of water, respectively, κ the hygroscopicity parameter, and $d_{p,c}$ is the critical dry diameter corresponding to the critical supersaturation. Following *Moore et al.* (2011), Equation 7 can be rearranged to express the number of particles with composition κ and size larger than the critical diameter $d_{p,c}$ that will act as CCN when exposed to some supersaturation. Assuming the aerosol to be internally mixed, κ can be calculated by determining the $d_{p,c}$ from which integrating the aerosol size distribution will give the measured CCN number concentration,

$$N_{CCN}\left(ss\%\right) = \int_{d_{p,c}}^{\infty} n_{CN} dD_p \tag{8}$$

where $N_{CCN}\left(ss\%\right)$ is the CCN number concentration as a function of supersaturation, $d_{p,c}$ is the dry particle diameter, and n_{CN} is the particle size distribution function. Using the critical supersaturation and dry diameter found using Equation 8, Equation 7 can be use to calculate the associated κ value. Since the CCN number concentration measurements were made sampling total aerosol number as opposed to size-selected aerosol, the calculated κ values are most representative of the aerosol around the size of $d_{p,c}$, since those CCN from those aerosol would be the most sensitive to changes in κ (*Moore et al.*, 2012).

Figure 3.6 shows the median CCN-derived κ values plotted as a function of their corresponding $d_{p,c}$. Markers are colored by supersaturation bin. Error bars represent the interquartile range of calculated $d_{p,c}$ and κ values. Throughout the region, the accumulation mode aerosol shows low CCN-derived hygroscopicity of about 0.2 reflecting the dominance of organics in the aerosol. As higher supersaturations start activating smaller particles, the CCN-derived hygroscopicities start to increase, suggesting the Aitken mode aerosol is dominated by inorganic compounds. The variability in κ for the Aitken mode aerosol is much larger than that observed for the accumulation mode aerosol, possibly due to the increased sensitivity of $d_{p,c}$ on CCN number concentration in the Aitken mode. Size distributions between 4–70 nm are produced using a non-linear inversion technique using data from the NMASS and the UHSAS (*Brock et al.*, 2000). During the Aerosol, Radiation, and Cloud Processes affecting Arctic Climate (ARCPAC) project of April 2008, the mean deviation for particle number in the NMASS size range was a positive bias of +2.8% with a standard

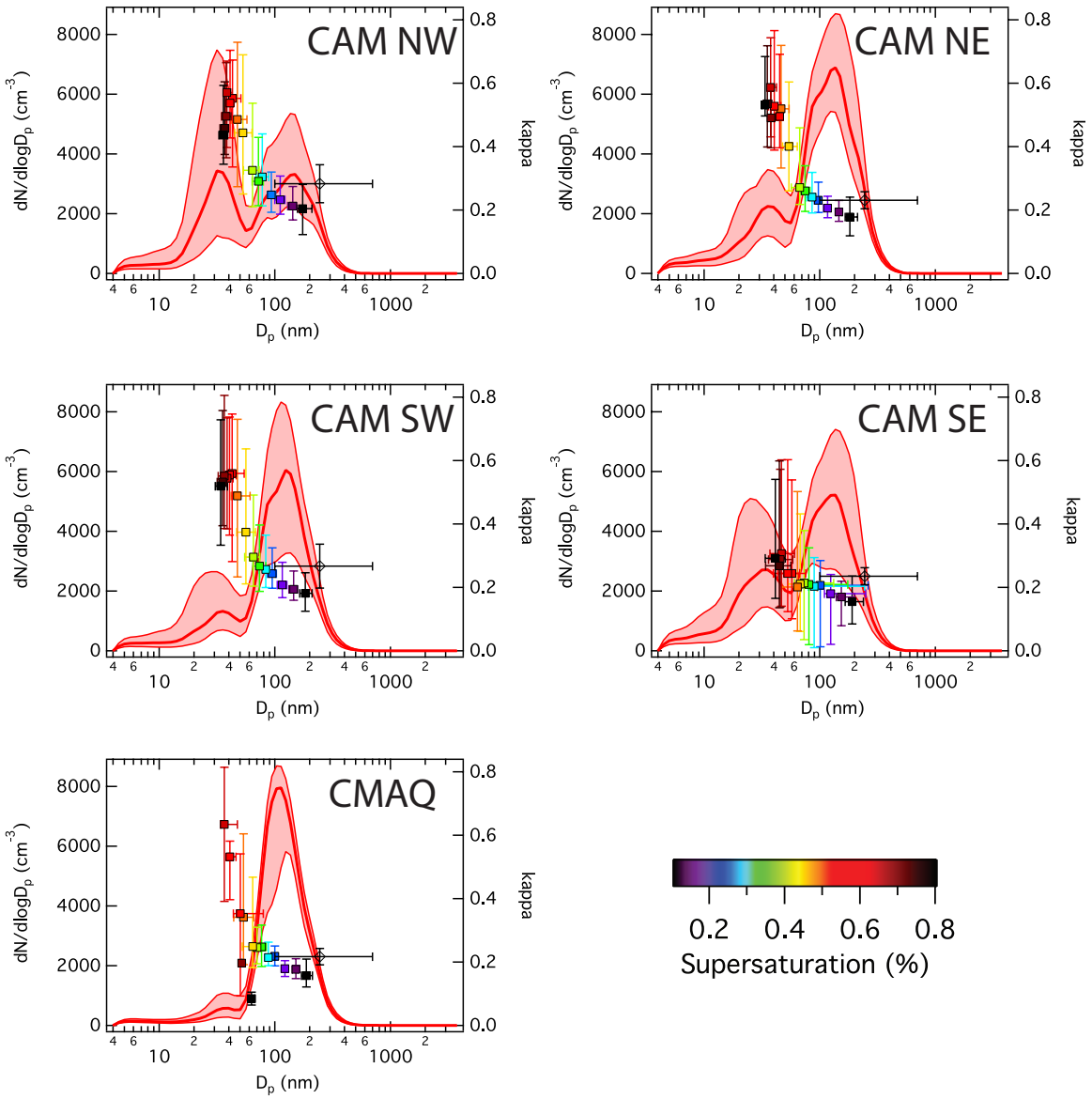

Figure 3.6: CCN-derived aerosol hygroscopicity form measurements aboard the WP-3D colored by supersaturation along with hygroscopicity calculated from aerosol bulk composition. Also shown are measured median size distributions with interquartile ranges.

deviation of 8.6%. This led to an uncertainty in total particle number in the NMASS size range of +5.8%/-11.4%. Any systematic biases from the inversion method will be magnified in the calculation of κ since $\kappa \sim d_{p,c}^{-3}$.

Shown for comparison in Figure 3.6 are the κ values calculated from bulk AMS measurements as detailed in Section 3.2.2.2. The error bar in diameter represents the size range over which the C-ToF-AMS samples particles at 100% efficiency while the error bar in κ space represents the standard deviation of κ values calculated from bulk AMS composition. The absence of refractory species is not expected to significantly alter the calculated κ. For the overlapping size ranges, there is good agreement between the AMS-derived and CCN-derived κ values.

3.3.5 Updraft velocity

The dependence of cloud droplet number concentration (CDNC) on updraft velocity poses a challenge to parameterizations of CDNC since cloud-scale updraft velocities are not resolved at the resolution of global climate models. One solution is to assume that a characteristic updraft velocity can be derived from the probability density function (PDF) that represents all updraft velocities that occur within a GCM grid cell. This representative updraft velocity is used to calculate CDNC in the grid cell. Previous studies (*Conant et al.*, 2004; *Meskhidze et al.*, 2005; *Peng et al.*, 2005; *Fountoukis et al.*, 2007) using this approach to predict CDNC at cloud base in warm clouds have found a suitable characteristic updraft velocity to be the 0.8σ, where σ is the width of the PDF of updraft velocities. Measured updraft velocities from the WP-3D are used to calculate characteristic updraft velocities used to drive the AG00 parameterization. Histograms of measured updraft velocities along with PDFs fit to those histograms are shown in Figure 3.7.

3.3.6 Droplet number concentrations and sensitivity

A summary of the inputs used to drive AG00 is shown in Figure 3.4. For the inputs derived from measurements, the input temperature and pressure are the average temperature and pressure when the WP-3D was sampling in the corresponding grid cell at pressures greater than 900 mb. The characteristic updraft, w^*, is computed from the PDF of updraft velocities

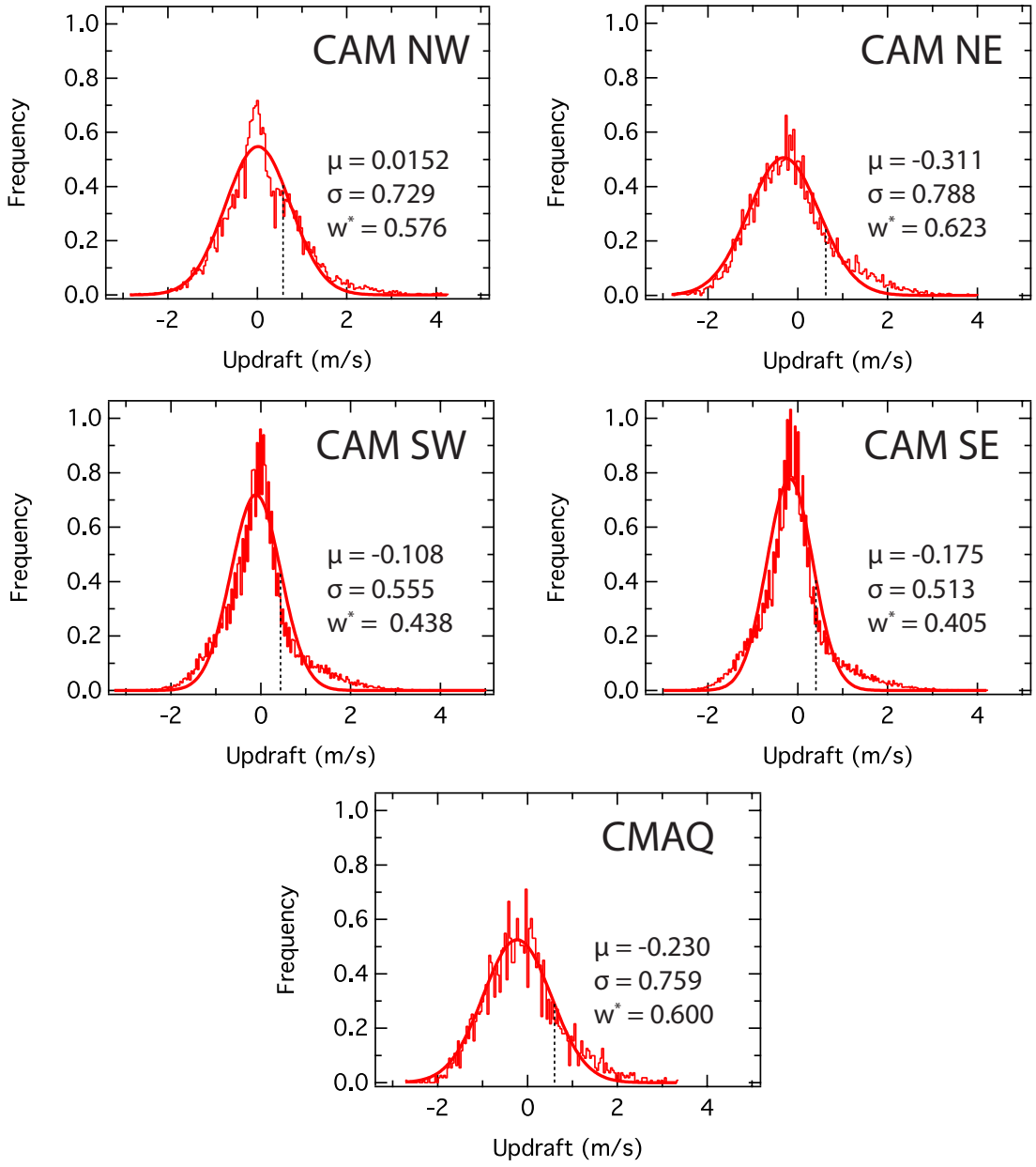

Figure 3.7: Histograms of updraft velocities measured by the WP-3D with PDF fits. The characteristic updraft velocity w^* is taken to be 0.8σ.

Table 3.4: Meteorological and aerosol inputs used to drive the AG00 parameterization.

Measurement state											
Grid cell	T	P	w*	Aitken				Accumulation			
	(K)	(mb)	(m/s)	N_a (cm^{-3})	D_{pg} (nm)	σ	κ	N_a (cm^{-3})	D_{pg} (nm)	σ	κ
CAM NE	296.32	931.00	0.623	937.9	30.80	1.59	0.231	3464	127.4	1.59	0.231
CAM NW	294.22	934.61	0.576	1319	31.97	1.46	0.283	1781	134.3	1.63	0.283
CAM SE	295.72	932.07	0.405	1472	29.58	1.71	0.235	2579	126.4	1.57	0.235
CAM SW	296.77	941.29	0.438	488.4	29.42	1.48	0.267	2804	121.6	1.53	0.267
CMAQ	297.23	942.23	0.600	123.0	30.54	1.25	0.217	3362	114.7	1.48	0.217
Model state											
Grid cell	T	P	w*	Aitken				Accumulation			
	(K)	(mb)	(m/s)	N_a (cm^{-3})	D_{pg} (nm)	σ	κ	N_a (cm^{-3})	D_{pg} (nm)	σ	κ
CAM NE	294.21	936.20	0.398	62.44	49.27	1.6	0.338	549.6	184.6	1.8	0.260
CAM NW	295.25		0.403	48.90	48.40		0.335	484.4	183.3		0.257
CAM SE	295.22		0.364	65.28	49.66		0.323	597.2	188.8		0.248
CAM SW	295.73		0.373	45.30	49.17		0.329	553.0	182.0		0.252
CMAQ	284.83	900	0.227	308.3	26.54	2.18	0.500	273.15	99.56	2.08	0.371

fit to histograms of updraft velocities measured by the WP-3D. Lognormal distributions fit to the median measured size distributions provide the aerosol number, geometric mean diameter, and geometric standard deviation of each mode. No significant amount of coarse mode aerosol was measured so the contribution of coarse mode aerosol number to total droplet number is not included. All aerosol modes are assumed to be internally mixed with the AMS-derived kappa values representing the hygroscopicity of both modes.

For the inputs computed by the models, the input temperature and pressure are the averages of the temperature and pressures of the model vertical layers being considered. Aerosol number, geometric mean diameter, geometric standard deviation, and hygroscopicity for each mode are averages of daily averages from each model's simulation period. Since the coarse mode aerosol contributes negligibly to total modeled aerosol number, the contribution of coarse mode aerosol number to total droplet number is also not included to be consistent with the inputs from the measurement data. Average updraft velocities in the model grid cells were used as characteristic updraft velocities. Since most of the sampling done by the WP-3D was during the day, the characteristic updraft velocities derived from the aircraft measurements are significantly higher than those computed by the models, which are 24 hour averages. Table 3.5 shows the difference in droplet number when using characteristic updraft velocities from measurements versus from models. Using modeled aerosol inputs

Table 3.5: Cloud droplet number N_d calculated from different inputs.

	N_d (cm^{-3})				
Input source	CAM NE	CAM NW	CAM SE	CAM SW	CMAQ
Measurements	913.500	737.670	549.393	612.354	764.428
Models	349.184	317.805	357.958	338.149	119.245
Models, measured w*	403.059	354.774	373.020	358.464	177.585

and characteristic updraft velocities derived from the aircraft measurements give cloud droplet number concentrations closer to those calculated with measured aerosol inputs and characteristic updraft velocities. In order to focus on the aerosol impacts on cloud droplet number, results will focus on cloud droplet number and sensitivities using characteristic updraft velocities derived from aircraft measurements. Table 3.5 also shows that although total aerosol number measured aboard the WP-3D is about four times greater than that calculated by the models, the resulting difference in cloud droplet number produced using the measurement characteristic updraft velocity is only twice as much.

The change in N_d attributable to changes in χ_j can be approximated to first order as

$$(\Delta N_d)_{\chi_j} \approx \left(\frac{\partial N_d}{\partial \chi_j}\right)_{model} \times \Delta\chi_j. \tag{9}$$

The sensitivity $\frac{\partial N_d}{\partial \chi_j}$ is calculated for the input parameters defining the model state and is assumed to be constant. While the sensitivities do vary between the model and measurement states, the magnitude of ΔN_d is expected to largely be controlled by $\Delta\chi_j$, the change in the aerosol property (*Morales Betancourt and Nenes*, 2014). The changes in droplet number attributable to changes in individual aerosol properties are shown in Figure 3.8.

The difference in droplet number is largely controlled by the properties of the accumulation mode aerosol. This is expected since the accumulation mode aerosol activate into cloud droplets before the Aitken mode aerosol. Figure 3.6 shows that up until about supersaturations of about 0.4%, activation of CCN into cloud droplets in largely contained to the accumulation mode aerosol. Within the accumulation mode aerosol parameters, the aerosol number is the overwhelmingly dominant factor. After the aerosol number, the next important contributor toΔN_d are the mode diameter D_{pg} and the mode width σ.

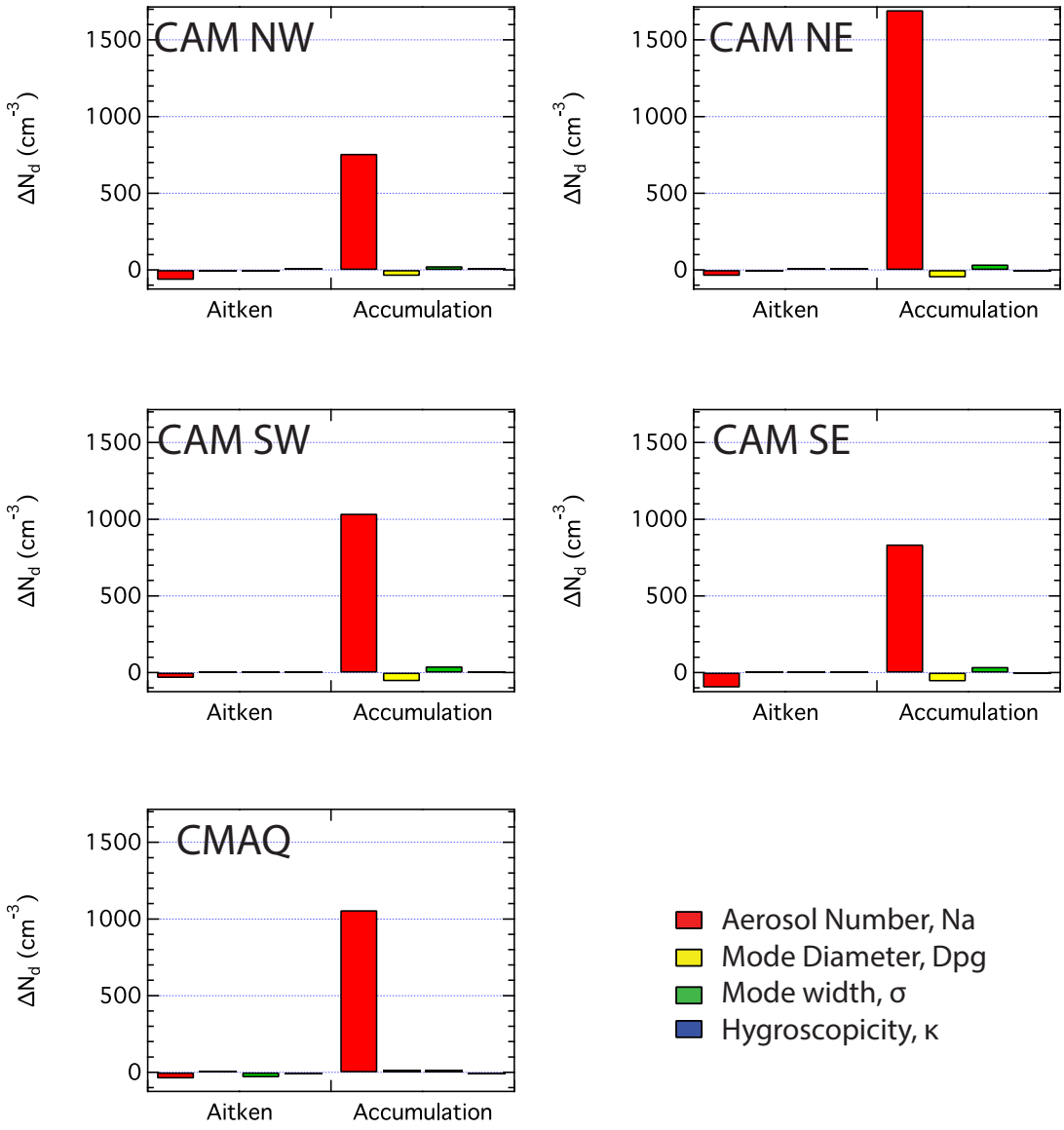

Figure 3.8: Difference in N_d between modeled and measured inputs attributed to input parameters.

3.4 Conclusions

Measurements of aerosol size, composition, CCN activity, and aerosol hygroscopicity in the southeastern United States from the SENEX 2013 project are analyzed and presented here. Aerosol in the southeastern United States is dominated by organics with a prominent inorganic-dominated Aitken mode peak. Maximum CCN activation fractions of 90% were observed starting at around 0.6% supersaturation, with generally good agreement between aircraft and ground measurements. Good agreement between aerosol hygroscopicity derived from CCN and AMS bulk measurements suggest the aerosol to be internally mixed.

Measurements of aerosol properties were compared to those predicted by the CAM and CMAQ models. CAM was able to adequately reproduce aerosol composition while CMAQ was unable to. Both models struggled to accurately reproduce the observed aerosol size distributions, although the total aerosol mass computed by CAM was close to those observed on the aircraft. The AG00 cloud droplet parameterization was used to calculate the cloud droplet number at the conditions defined by the measurements and models. Even though observed aerosol number was five times higher than produced in either model, calculated droplet number from measured data was only about two times higher than calculated from model data. Most of the difference in both droplet number and CCN spectra is driven by the difference in aerosol number in the accumulation mode. Increased droplet numbers calculated from measured data provide additional cooling compared to that calculated from the model, which could have an impact of the assessment of the climate impacts in the southeastern United States.

CHAPTER IV

CONCLUSIONS AND FUTURE DIRECTIONS

4.1 Conclusions

Measurements of the ability of atmospheric aerosol to act as cloud condensation nuclei are necessary to constrain the uncertainty associated with aerosol-cloud interactions. The introduction of the Droplet Measurement Technologies Continuous-Flow Streamwise Thermal Gradient Cloud Condensation Nuclei chamber (*Roberts and Nenes*, 2005; *Lance et al.*, 2006) allowed for widespread, reliable measurements of CCN activity. The development of Scanning Flow CCN Analysis (*Moore and Nenes*, 2009) expanded the capabilities of the CFSTGC to rapidly measure CCN spectra across a range of supersaturations, reducing the time necessary to obtain CCN spectra from one hour down to as fast as ten seconds. In Chapter 2, hardware improvements to the SFCA technique and extensive laboratory and model characterization of SFCA were presented. The use of an Arduino microcontroller with a mass flow controller to control the flow rate in the CFSTGC gives greater flexibility and control over the supersaturation generated in the instrument. A set of calibration experiments were carried out to explore the dependence of instrument supersaturation on instrument pressure, flow rate waveform, and flow rate wave period. The range of supersaturations generated in the CFSTGC during SFCA decreases with decreasing instrument pressure while it increases with decreasing flow rate wave period. A change in flow rate waveform from the conventional triangle wave to a sinusoidal wave increased the supersaturation range over the same flow rate range. Simulations using the full CFSTGC model showed that instrument calibrations were largely able accurately capture the supersaturations generated during flight conditions. Most of the deviations from the calibrations resulted from deviations in flow rate ranges and column top temperature.

The Arduino+MFC module has been flown on four airborne field deployments to good results. The results from the Southeast Nexus (SENEX) field campaign were presented

here. SENEX was a part of the Southeast Atmosphere Study (SAS), a broad effort in the summer of 2013 to comprehensively characterize the meteorology, chemistry, and aerosol in the southeastern United States. SAS was partly motivated by the anomalous cooling trend observed in the southeastern United States over the past fifty years. Aerosol size and composition, CCN activity, and cloud droplet number where characterized from data measured aboard the National Oceanic and Atmospheric Administration (NOAA) WP-3D aircraft and evaluated against simulations using the Community Atmosphere Model (CAM) and Community Multi-scale Air Quality Model (CMAQ). Aerosol in the southeastern United States was found to mostly composed of organics, but the composition of Aitken mode aerosol was found to have hygroscopicity similar to pure inorganic compounds. Both models fail to capture key characteristics of the observed aerosol, in particular, largely underestimating the total aerosol number. Under typical observed updraft values, however, the resulting cloud droplet number is only underestimated by a factor of two. Using the sensitivities of cloud droplet number to relevant input parameters, it was determined that the primary driver of discrepancy between the cloud droplet number computed from the observed and modeled aerosol parameters is the total aerosol number.

4.2 Future directions

As revealed from model simulations, SFCA instrument supersaturation during flight conditions can deviate from the supersaturation ranges derived from calibrations done on the ground. Changes in ambient pressure and temperature during airborne ambient sampling can affect the performance of the mass flow controller dictating the flow rate in the CFSTGC. One solution is to use instrument temperature and pressure measurements in a control feedback loop to take into account those effects on flow rate. Alternatively, a volumetric flow controller such as an Alicat Scientific MC-5SLPM can be employed.

Two different SFCA waveforms were tested in Chapter 2: triangle waves used during conventional operation of SFCA and sinusoidal waves made possible by use of the mass flow controller. The control and flexibility afforded by the mass flow controller allows for additional waveforms to be employed during SFCA. A few possible potential waveforms are shown in

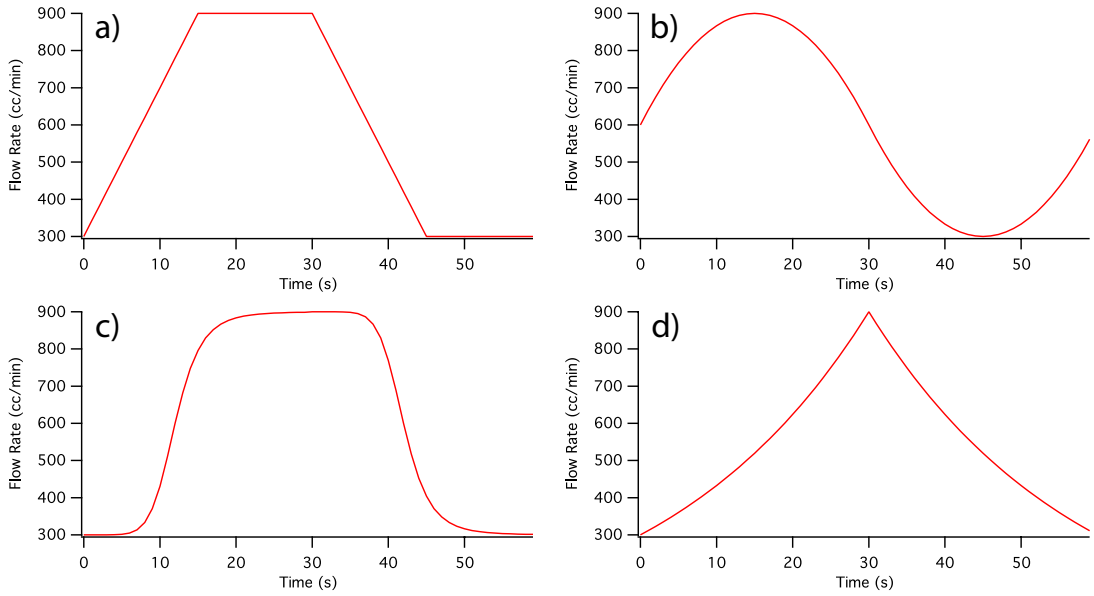

Figure 4.1: Other potential waveforms. a) Trapezoid, b) piecewise second-order polynomial, c) piecewise sigmoids, and d) piecewise exponentials.

Figure 4.1. Since the supersaturation in the CFSTGC generated during SFCA operation is a function of the change in flow rate, each waveform is expected to have a different relationship between instrument supersaturation and flow rate. In particular, the piecewise sigmoidal waveform provides a great deal of flexibility. The location of the inflection point and the steepness of the sigmoid slope can both be adjusted to focus on specific supersaturation ranges of interest.

In Chapter 3, measurements of CCN-derived aerosol hygroscopicity found that smaller aerosol in the Aitken mode have hygroscopicity approaching those of purely inorganic compounds. This could be due to new particle formation from sulfur dioxide emissions and sulfate emissions from power plants. This hypothesis may be tested by correlating measurements of SO_2 mixing ratio with total aerosol number less than 70 nm. It may also be tested by geographically correlating amount of Aitken mode aerosol to regions downwind of power plants. Size-resolved AMS mass loadings may also provide evidence of enhancement of sulfate at smaller aerosol diameters.

Cloud droplet numbers were calculated from aerosol properties measured aboard the WP-3D and simulated from models. The next step is to calculated the radiative balance

associated with the cloud droplet numbers. If historic measurements of aerosol size and composition are available, it would be possible to calculate a radiative forcing between the present and the time of the historic measurements. This would provide a basis for comparison for cloud radiative forcing calculated from models.

Using the sensitivities of cloud droplet number to its input parameters, the change in droplet number attributable to the difference between measured and modeled input parameters was assessed. These calculations help to show in what areas the model need to improve in order to more accurately predict cloud droplet number. While cloud droplet number is sensitive to aerosol kappa values at the modeled aerosol state, both models manage to calculate aerosol composition well enough for the contribution of kappa value to change in droplet value to be small. Differences in total aerosol number is the overwhelming contributor to the differences seen in cloud droplet number. In the case of CAM, the total aerosol mass is very close to that measured aboard the WP-3D. However, too much mass is in the coarse mode, so consequently, not enough mass or number is present in the accumulation mode. In the case of CMAQ, not enough aerosol mass is produced to match that measured aboard the WP-3D. That ability of model to correctly produce an aerosol number distribution will bring about the greatest improvement in cloud droplet number prediction. This in turn will contribute to a more accurate assessment of the impact of aerosol-cloud interactions on climate.

APPENDIX A

SFCA MODULE ARDUINO CODE

```
// Example Arduino code for sinusoid wave with a 30 second period at 600 mb.
float p = 30;
float pi = 3.1416;

void setup () {
  Serial.begin(9600);
  pinMode(13, OUTPUT);
  pinMode(6, OUTPUT);    // sets the pin as output
  analogWrite(6, (floor(84 + cos(2*pi*0/p)*56))); // Initial control signal
}

void loop () {
  while (1) {       // Enter waveform loop
  for (int t = 0; t<p; t++) {

   analogWrite(6, (floor(84 + cos(2*pi*t/p)*56)));
   delay(1000);

   Serial.print("I sent: ");
   Serial.print((floor(84 + cos(2*pi*t/p)*56))/255*5);
   Serial.print("    ");
   Serial.print("I got: ");
   Serial.println((float)analogRead(A1)/1023*5);
  }
  }
}
```

```
// Example Arduino code for triangle waves with 120 second period at 600 mb.
float p = 120;
float pi = 3.1415;


void setup () {
  Serial.begin(9600);
  pinMode(13, OUTPUT);
  pinMode(6, OUTPUT);    // sets the pin as output
  analogWrite(6, 84); // Initial control signal
}

void loop () {

  while (1) {       // Enter waveform loop
  for (int t = 0; t<p; t++) {

   analogWrite(6, (floor(84-56*((4.0/p)*(t-(p/2.0)*floor((float(t)/(p/2.0))
    +0.5)))*pow(-1, floor((float(t)/(p/2.0))+0.5)))));

   delay(1000);
   Serial.print("I sent: ");
   Serial.print((floor(84-56*((4.0/p)*(t-(p/2.0)*floor((float(t)/(p/2.0))+0.5)
    ))*pow(-1, floor((float(t)/(p/2.0))+0.5))))/255*5);
   Serial.print("     ");
   Serial.print("I got: ");
   Serial.println((float)analogRead(A1)/1023*5);
  }
  }
}
```

APPENDIX B

FIELD MISSION PARTICIPATION

Table B.1: List of field mission participation during PhD studies.

Field Campaign	Platform	Location	Dates
CalNex	CIRPAS Twin Otter	Ontario, CA	4 May — 28 May 2010
CalWater	PNNL G1	Sacramento, CA	2 February — 6 March 2011
EPEACE	CIRPAS Twin Otter	Marina, CA	8 July — 18 August 2011
DC3	NASA DC-8	Salina, KS	18 May — 22 June 2012
DISCOVER-AQ –San Joaquin Valley	NASA P-3B	Palmdale, CA	16 January — 6 February 2013
SENEX[a]	NOAA WP-3D	Smyrna, TN	10 June — 10 July 2013
SEAC^{4}RS[a]	NASA DC-8	Houston, TX	6 August — 23 September 2013
DISCOVER-AQ [a] –Houston	NASA P-3B	Houston, TX	4 September — 26 September 2013

[a] Field missions using the Arduino+MFC module to run SFCA.

References

Abdul-Razzak, H., and S. J. Ghan (2000), A parameterization of aerosol activation 2. Multiple aerosol types, *Journal of Geophysical Research*, *105*(D5), 6837–6844.

Albrecht, B. A. (1989), Aerosols, Cloud Microphysics, and Fractional Cloudiness, *Science*, *245*(4923), 1227–1230.

Allan, J. D., A. E. Delia, H. Coe, K. N. Bower, M. R. Alfarra, J. L. Jimenez, A. M. Middlebrook, F. Drewnick, T. B. Onasch, M. R. Canagaratna, J. T. Jayne, and D. R. Worsnop (2004), A generalised method for the extraction of chemically resolved mass spectra from Aerodyne aerosol mass spectrometer data, *Journal of Aerosol Science*, *35*(7), 909–922.

Andreae, M. O., and P. J. Crutzen (1997), Atmospheric Aerosols: Biogeochemical Sources and Role in Atmospheric Chemistry, *Science*, *276*(5315), 1052–1058.

Andreae, M. O., and D. Rosenfeld (2008), Aerosol–cloud–precipitation interactions. Part 1. The nature and sources of cloud-active aerosols, *Earth-Science Reviews*, *89*(1-2), 13–41.

Asa-Awuku, A., and A. Nenes (2007), Effect of solute dissolution kinetics on cloud droplet formation: Extended Köhler theory, *Journal of Geophysical Research*, *112*(D22).

Asa-Awuku, A., G. J. Engelhart, B. H. Lee, S. N. Pandis, and A. Nenes (2009), Relating CCN activity, volatility, and droplet growth kinetics of β-caryophyllene secondary organic aerosol, *Atmospheric Chemistry and Physics*, *9*, 795–812.

Asa-Awuku, A., A. Nenes, S. Gao, R. C. Flagan, and J. H. Seinfeld (2010), Water-soluble SOA from Alkene ozonolysis: composition and droplet activation kinetics inferences from analysis of CCN activity, *Atmospheric Chemistry and Physics*, *10*, 1585–1597.

Binkowski, F. S. (2003), Models-3 Community Multiscale Air Quality (CMAQ) model aerosol component 1. Model description, *Journal of Geophysical Research*, *108*(D6), 4183.

Blando, J. D., and B. J. Turpin (2000), Secondary organic aerosol formation in cloud and fog droplets: a literature evaluation of plausibility, *Atmospheric Environment*, *34*(10), 1623–1632.

Blando, J. D., R. J. Porcja, T.-H. Li, D. Bowman, P. J. Lioy, and B. J. Turpin (1998), Secondary Formation and the Smoky Mountain Organic Aerosol: An Examination of Aerosol Polarity and Functional Group Composition During SEAVS, *Environmental Science & Technology*, *32*(5), 604–613.

Boucher, O., D. Randall, P. Artaxo, C. Bretherton, G. Feingold, P. Forster, V.-M. Kerminen, Y. Kondo, H. Liao, U. Lohmann, P. Rasch, S. Satheesh, S. Sherwood, B. Stevens, and X. Zhang (2013), *Clouds and Aerosols*, book section 7, pp. 571–658, Cambridge University Press, Cambridge, United Kingdom and New York, NY, USA, doi:10.1017/CBO9781107415324.016.

Bougiatioti, A., C. Fountoukis, N. Kalivitis, S. N. Pandis, A. Nenes, and N. Mihalopoulos (2009), Cloud condensation nuclei measurements in the marine boundary layer of the eastern Mediterranean: CCN closure and droplet growth kinetics, *Atmospheric Chemistry and Physics*, *9*, 7053–7066.

Bougiatioti, A., A. Nenes, C. Fountoukis, N. Kalivitis, S. N. Pandis, and N. Mihalopoulos (2011), Size-resolved CCN distributions and activation kinetics of aged continental and marine aerosol, *Atmospheric Chemistry and Physics*, *11*(16), 8791–8808.

Brock, C. A., F. Schröder, B. Kärcher, A. Petzold, R. Busen, and M. Fiebig (2000), Ultrafine particle size distributions measured in aircraft exhaust plumes, *Journal of Geophysical Research*, *105*(D21), 26,555–26,567.

Brock, C. A., J. Cozic, R. Bahreini, K. D. Froyd, A. M. Middlebrook, A. McComiskey, J. Brioude, O. R. Cooper, A. Stohl, K. C. Aikin, J. A. de Gouw, D. W. Fahey, R. A. Ferrare, R. S. Gao, W. Gore, J. S. Holloway, G. Hübler, A. Jefferson, D. A. Lack, S. Lance, R. H. Moore, D. M. Murphy, A. Nenes, P. C. Novelli, J. B. Nowak, J. A. Ogren, J. Peischl, R. B. Pierce, P. Pilewskie, P. K. Quinn, T. B. Ryerson, K. S. Schmidt, J. P. Schwarz, H. Sodemann, J. R. Spackman, H. Stark, D. S. Thomson, T. Thornberry, P. Veres, L. A. Watts, C. Warneke, and A. G. Wollny (2011), Characteristics, sources, and transport of aerosols measured in spring 2008 during the aerosol, radiation, and cloud processes affecting Arctic Climate (ARCPAC) Project, *Atmospheric Chemistry and Physics*, *11*(6), 2423–2453.

Butler, A. J. (2003), Daily sampling of PM 2.5in Atlanta: Results of the first year of the Assessment of Spatial Aerosol Composition in Atlanta study, *Journal of Geophysical Research*, *108*(D7), 8415.

Byun, D., and K. L. Schere (2006), Review of the Governing Equations, Computational Algorithms, and Other Components of the Models-3 Community Multiscale Air Quality (CMAQ) Modeling System, *Applied Mechanics Reviews*, *59*(2), 51.

Canagaratna, M. R., J. T. Jayne, J. L. Jimenez, J. D. Allan, M. R. Alfarra, Q. Zhang, T. B. Onasch, F. Drewnick, H. Coe, A. Middlebrook, A. Delia, L. R. Williams, A. M. Trimborn, M. J. Northway, P. F. DeCarlo, C. E. Kolb, P. Davidovits, and D. R. Worsnop (2007), Chemical and microphysical characterization of ambient aerosols with the aerodyne aerosol mass spectrometer, *Mass Spectrometry Reviews*, *26*(2), 185–222.

Carlton, A. G., and B. J. Turpin (2013), Particle partitioning potential of organic compounds is highest in the Eastern US and driven by anthropogenic water, *Atmospheric Chemistry and Physics*, *13*(20), 10,203–10,214.

Cerully, K. M., A. Bougiatioti, J. R. Hite, Jr., H. Guo, L. Xu, N. L. Ng, R. Weber, and A. Nenes (2015), On the link between hygroscopicity, volatility, and oxidation state of ambient and water-soluble aerosols in the southeastern United States, *Atmospheric Chemistry and Physics*, *15*(15), 8679–8694.

Chameides, W., R. Lindsay, J. Richardson, and C. Kiang (1988), The role of biogenic hydrocarbons in urban photochemical smog: Atlanta as a case study, *Science*, *241*(4872), 1473–1475, doi:10.1126/science.3420404.

Chu, S. H., J. Hemby, B. Cox, R. Scheffe, and N. Meyer (1996), Photochemical assessment monitoring stations: 1996 data analysis results report, EPA-454/R-96-006, Environmental Protection Agency, Office of Air Quality Planning and Standards, Research Triangle Park, North Carolina.

Conant, W. C., T. M. VanReken, T. A. Rissman, V. Varutbangkul, H. H. Jonsson, A. Nenes, J. L. Jimenez, A. E. Delia, R. Bahreini, G. C. Roberts, R. C. Flagan, and J. H. Seinfeld (2004), Aerosol–cloud drop concentration closure in warm cumulus, *Journal of Geophysical Research*, *109*(D13), D13,204.

Cowling, E. B., W. L. Chameides, C. S. Kiang, F. C. Fehsenfeld, and J. F. Meagher (1998), Introduction to special section: Southern Oxidants Study Nashville/Middle Tennessee Ozone Study, *Journal of Geophysical Research*, *103*(D17), 22,209–22,212.

Cubison, M. J., B. Ervens, G. Feingold, K. S. Docherty, I. M. Ulbrich, L. Shields, K. A. Prather, S. Hering, and J. L. Jiminez (2008), The influence of chemical composition and mixing state of Los Angeles urban aerosol on CCN number and cloud properties, *Atmospheric Chemistry and Physics*, *8*, 5649–5667.

de Gouw, J. A., A. M. Middlebrook, C. Warneke, P. D. Goldan, W. C. Kuster, J. M. Roberts, F. C. Fehsenfeld, D. R. Worsnop, M. R. Canagaratna, A. A. P. Pszenny, W. C. Keene, M. Marchewka, S. B. Bertman, and T. S. Bates (2005), Budget of organic carbon in a polluted atmosphere: Results from the New England Air Quality Study in 2002, *Journal of Geophysical Research*, *110*(D16), D16,305.

Engelhart, G. J., A. Asa-Awuku, A. Nenes, and S. N. Pandis (2008), CCN activity and droplet growth kinetics of fresh and aged monoterpene secondary organic aerosol, *Atmospheric Chemistry and Physics*, *8*, 3937–3949.

Ervens, B., B. J. Turpin, and R. J. Weber (2011), Secondary organic aerosol formation in cloud droplets and aqueous particles (aqSOA): a review of laboratory, field and model studies, *Atmospheric Chemistry and Physics*, *11*(21), 11,069–11,102.

Facchini, M. C., M. Mircea, S. Fuzzi, and R. J. Charlson (1999), Cloud albedo enhancement by surface-active organic solutes in growing droplets, *Nature*, *401*, 257–259.

Forster, P., V. Ramaswamy, P. Artaxo, T. Berntsen, R. Betts, D. W. Fahey, J. Haywood, J. Lean, D. C. Lowe, G. Myhre, J. Nganga, R. Prinn, G. Raga, M. Schulz, and R. Van Dorland (2007), Changes in Atmospheric Constituents and in Radiative Forcing, in *Climate Change 2007: The Physical Science Basis. Contribution of Working Group I to the Fourth Assessment Report of the Intergovermental Panel on Climate Change*, pp. 1–106, Cambridge University Press.

Fountoukis, C., A. Nenes, N. Meskhidze, R. Bahreini, W. C. Conant, H. Jonsson, s. murphy, A. Sorooshian, V. Varutbangkul, F. Brechtel, R. C. Flagan, and J. H. Seinfeld (2007), Aerosol–cloud drop concentration closure for clouds sampled during the International Consortium for Atmospheric Research on Transport and Transformation 2004 campaign, *Journal of Geophysical Research*, *112*(D10), D10S30.

George, I. J., and J. P. D. Abbatt (2010), heterogeneous oxidation of atmospheric aerosolparticles by gas-phase radicals, *Nature Publishing Group*, *2*(9), 713–722.

Goldstein, A. H., C. D. Koven, C. L. Heald, and I. Y. Fung (2009), Biogenic carbon and anthropogenic pollutants combine to form a cooling haze over the southeastern United States, *Proceedings of the National Academy of Sciences*, *106*(22), 8835–8840.

Hand, J. L., R. B. Ames, S. M. Kreidenweis, D. E. Day, and W. C. Malm (2000), Estimates of Particle Hygroscopicity during the Southeastern Aerosol and Visibility Study, *Journal of the Air & Waste Management Association*, *50*(5), 677–685.

Hennigan, C. J., M. H. Bergin, A. G. Russell, A. Nenes, and R. J. Weber (2009), Gas/particle partitioning of water-soluble organic aerosol in Atlanta, *Atmospheric Chemistry and Physics*, *9*, 3613–3628.

Hersey, S. P., J. S. Craven, A. R. Metcalf, J. Lin, T. Lathem, K. J. Suski, J. F. Cahill, H. T. Duong, A. Sorooshian, H. H. Jonsson, M. Shiraiwa, A. Zuend, A. Nenes, K. A. Prather, R. C. Flagan, and J. H. Seinfeld (2013), Composition and hygroscopicity of the Los Angeles Aerosol: CalNex, *Journal of Geophysical Research: Atmospheres*, pp. 3016–3036.

Hidy, G. M., C. L. Blanchard, K. Baumann, E. Edgerton, S. Tanenbaum, S. Shaw, E. Knipping, I. Tombach, J. Jansen, and J. Walters (2014), Chemical climatology of the southeastern United States, 1999-2013, *Atmospheric Chemistry and Physics*, *14*(21), 11,893–11,914.

Hildebrandt Ruiz, L., A. L. Paciga, K. M. Cerully, A. Nenes, N. M. Donahue, and S. N. Pandis (2015), Formation and aging of secondary organic aerosol from toluene: changes in chemical composition, volatility, and hygroscopicity, *Atmospheric Chemistry and Physics*, *15*(14), 8301–8313.

Holland, D., R. Baumgardner, T. Haas, and G. Oehlert (1995), *Design of the Clean Air Act deposition monitoring network. (Chapter 7)*.

Hoyle, C. R., G. Myhre, T. K. Berntsen, and I. S. A. Isaksen (2009), Anthropogenic influence on SOA and the resulting radiative forcing, *Atmospheric Chemistry and Physics*, *9*, 2715–2728.

IPCC (2013), *Summary for Policymakers*, book section SPM, pp. 1–30, Cambridge University Press, Cambridge, United Kingdom and New York, NY, USA, doi: 10.1017/CBO9781107415324.004.

Jayne, J. T., D. C. Leard, X. Zhang, P. Davidovits, K. A. Smith, C. E. Kolb, and D. R. Worsnop (2000), Development of an Aerosol Mass Spectrometer for Size and Composition Analysis of Submicron Particles, *Aerosol Science and Technology*, *33*(1-2), 49–70.

Jimenez, J. L. (2003), Ambient aerosol sampling using the Aerodyne Aerosol Mass Spectrometer, *Journal of Geophysical Research*, *108*(D7), 8425.

Köhler, H. (1936), The Nucleus in and the Growth of Hygroscopic Droplets, *Transactions of the Faraday Society*, pp. 1152–1161.

Kokkola, H., M. Vesterinen, T. Anttila, A. Laaksonen, and K. E. J. Lehtinen (2008), Technical note: Analytical formulae for the critical supersaturations and droplet

diameters of CCN containing insoluble material, *Atmospheric Chemistry and Physics*, *8*, 1985–1988.

Kulmala, M., A. Laaksonen, P. Korhonen, T. Vesala, T. Ahonen, and J. C. Barrett (1993), The Effect of Atmospheric Nitric Acid Vapor on Cloud Condensation Nucleus Activation, *Journal of Geophysical Research*, *98*(D12), 22,949–22,958.

Kumar, P., I. N. Sokolik, and A. Nenes (2009), Parameterization of cloud droplet formation for global and regional models: including adsorption activation from insoluble CCN, *Atmospheric Chemistry and Physics*, *9*, 2517–2532.

Kuwata, M., Y. Kondo, Y. Miyazaki, Y. Komazaki, J. H. Kim, S. S. Yum, H. Tanimoto, and H. Matsueda (2008), Cloud condensation nuclei activity at Jeju Island, Korea in spring 2005, *Atmospheric Chemistry and Physics*, *8*, 2933–2948.

Laaksonen, A., P. Korhonen, M. Kulmala, and R. J. Charlson (1998), Modification of the Köhler equation to include soluble trace gases and slightly soluble substances., *Journal of the Atmospheric Sciences*, *55*, 853–862.

Lamarque, J. F., T. C. Bond, V. Eyring, C. Granier, A. Heil, Z. Klimont, D. Lee, C. Liousse, A. Mieville, B. Owen, M. G. Schultz, D. Shindell, S. J. Smith, E. Stehfest, J. Van Aardenne, O. R. Cooper, M. Kainuma, N. Mahowald, J. R. McConnell, V. Naik, K. Riahi, and D. P. van Vuuren (2010), Historical (1850–2000) gridded anthropogenic and biomass burning emissions of reactive gases and aerosols: methodology and application, *Atmospheric Chemistry and Physics*, *10*(15), 7017–7039.

Lance, S., A. Nenes, J. Medina, and J. N. Smith (2006), Mapping the Operation of the DMT Continuous Flow CCN Counter, *Aerosol Science and Technology*, *40*(4), 242–254.

Lance, S., A. Nenes, C. Mazzoleni, M. K. Dubey, H. Gates, V. Varutbangkul, T. A. Rissman, S. M. Murphy, A. Sorooshian, R. C. Flagan, J. H. Seinfeld, G. Feingold, and H. H. Jonsson (2009), Cloud condensation nuclei activity, closure, and droplet growth kinetics of Houston aerosol during the Gulf of Mexico Atmospheric Composition and Climate Study (GoMACCS), *Journal of Geophysical Research*, *114*.

Legates, D. R., and C. J. Willmott (1990), Mean Seasonal and Spatial Variability in Gauge-Corrected, Global Precipitation, *International Journal of Climatology*, *10*, 111–127.

Leibensperger, E. M., L. J. Mickley, D. J. Jacob, W. T. Chen, J. H. Seinfeld, A. Nenes, P. J. Adams, D. G. Streets, N. Kumar, and D. Rind (2012a), Climatic effects of 1950-2050 changes in US anthropogenic aerosols - Part 1: Aerosol trends and radiative forcing, *Atmospheric Chemistry and Physics*, *12*(7), 3333–3348.

Leibensperger, E. M., L. J. Mickley, D. J. Jacob, W. T. Chen, J. H. Seinfeld, A. Nenes, P. J. Adams, D. G. Streets, N. Kumar, and D. Rind (2012b), Climatic effects of 1950-2050 changes in US anthropogenic aerosols - Part 2: Climate response, *Atmospheric Chemistry and Physics*, *12*(7), 3349–3362.

Liu, X., R. C. Easter, S. J. Ghan, R. Zaveri, P. Rasch, X. Shi, J. F. Lamarque, A. Gettelman, H. Morrison, F. Vitt, A. Conley, S. Park, R. Neale, C. Hannay, A. M. L. Ekman, P. Hess, N. Mahowald, W. Collins, M. J. Iacono, C. S. Bretherton, M. G. Flanner, and D. Mitchell (2012), Toward a minimal

representation of aerosols in climate models: description and evaluation in the Community Atmosphere Model CAM5, *Geoscientific Model Development*, *5*(3), 709–739.

Meskhidze, N., A. Nenes, W. C. Conant, and J. H. Seinfeld (2005), Evaluation of a new cloud droplet activation parameterization with in situ data from CRYSTAL-FACE and CSTRIPE, *Journal of Geophysical Research*, *110*(D16), D16,202.

Moore, R. H., and A. Nenes (2009), Scanning Flow CCN Analysis—A Method for Fast Measurements of CCN Spectra, *Aerosol Science and Technology*, *43*(12), 1192–1207.

Moore, R. H., R. Bahreini, C. A. Brock, K. D. Froyd, J. Cozic, J. S. Holloway, A. M. Middlebrook, D. M. Murphy, and A. Nenes (2011), Hygroscopicity and composition of Alaskan Arctic CCN during April 2008, *Atmospheric Chemistry and Physics*, *11*(22), 11,807–11,825.

Moore, R. H., K. Cerully, R. Bahreini, C. A. Brock, A. M. Middlebrook, and A. Nenes (2012), Hygroscopicity and composition of California CCN during summer 2010, *Journal of Geophysical Research*, *117*.

Moore, R. H., V. A. Karydis, S. L. Capps, T. L. Lathem, and A. Nenes (2013), Droplet number uncertainties associated with CCN: an assessment using observations and a global model adjoint, *Atmospheric Chemistry and Physics*, *13*(8), 4235–4251.

Morales Betancourt, R., and A. Nenes (2014), Understanding the contributions of aerosol properties and parameterization discrepancies to droplet number variability in a global climate model, *Atmospheric Chemistry and Physics*, *14*(9), 4809–4826.

Murphy, S. M., H. Agrawal, A. Sorooshian, L. T. Padró, H. Gates, S. Hersey, W. A. Welch, H. Jung, J. W. Miller, D. R. Cocker, III, A. Nenes, H. H. Jonsson, R. C. Flagan, and J. H. Seinfeld (2009), Comprehensive Simultaneous Shipboard and Airborne Characterization of Exhaust from a Modern Container Ship at Sea, *Environmental Science & Technology*, *43*(13), 4626–4640.

Myhre, G., D. Shindell, F.-M. Breòn, W. Collins, J. Fuglestvedt, J. Huang, D. Koch, J.-F. Lamarque, D. Lee, B. Mendoza, T. Nakajima, A. Robock, G. Stephens, T. Takemura, and H. Zhang (2013), *Anthropogenic and Natural Radiative Forcing*, book section 8, pp. 659–740, Cambridge University Press, Cambridge, United Kingdom and New York, NY, USA, doi:10.1017/CBO9781107415324.018.

Nguyen, T. K. V., M. D. Petters, S. R. Suda, H. Guo, R. J. Weber, and A. G. Carlton (2014), Trends in particle-phase liquid water during the Southern Oxidant and Aerosol Study, *Atmospheric Chemistry and Physics*, *14*(20), 10,911–10,930.

Padró, L. T., A. Asa-Awuku, R. Morrison, and A. Nenes (2007), Inferring thermodynamic properties from CCN activation experiments, *Atmospheric Chemistry and Physics*, *7*, 5263–5274.

Peng, Y., U. Lohmann, and R. Leaitch (2005), Importance of vertical velocity variations in the cloud droplet nucleation process of marine stratus clouds, *Journal of Geophysical Research*, *110*(D21), D21,213.

Petters, M. D., and S. M. Kreidenweis (2007), A single parameter representation of hygroscopic growth and cloud condensation nucleus activity, *Atmospheric Chemistry and Physics*, pp. 1961–1971.

Petters, M. D., C. M. Carrico, S. M. Kreidenweis, A. J. Prenni, P. J. DeMott, J. L. Collett, Jr., and H. Moosmüller (2009), Cloud condensation nucleation activity of biomass burning aerosol, *Journal of Geophysical Research*, *114*(D22).

Pincus, R., and M. B. Baker (1994), Effect of precipitation on the albedo susceptibility of clouds in the marine boundary layer, *Nature*, *372*, 250–252.

Portmann, R. W., S. Solomon, and G. C. Hegerl (2009), Spatial and seasonal patterns in climate change, temperatures, and precipitation across the United States, *Proceedings of the National Academy of Sciences*, *106*(18), 7324–7329.

Pringle, K. J., H. Tost, A. Pozzer, U. Pöschl, and J. Lelieveld (2010), Global distribution of the effective aerosol hygroscopicity parameter for CCN activation, *Atmospheric Chemistry and Physics*, *10*(12), 5241–5255.

Pye, H. O. T., R. W. Pinder, I. R. Piletic, Y. Xie, S. L. Capps, Y.-H. Lin, J. D. Surratt, Z. Zhang, A. Gold, D. J. Luecken, W. T. Hutzell, M. Jaoui, J. H. Offenberg, T. E. Kleindienst, M. Lewandowski, and E. O. Edney (2013), Epoxide Pathways Improve Model Predictions of Isoprene Markers and Reveal Key Role of Acidity in Aerosol Formation, *Environmental Science & Technology*, *47*(19), 11,056–11,064.

Raatikainen, T., R. H. Moore, T. L. Lathem, and A. Nenes (2012), A coupled observation – modeling approach for studying activation kinetics from measurements of CCN activity, *Atmospheric Chemistry and Physics*, *12*(9), 4227–4243.

Raatikainen, T., J. J. Lin, K. M. Cerully, T. L. Lathem, R. H. Moore, and A. Nenes (2014), CCN Data Interpretation Under Dynamic Operation Conditions, *Aerosol Science and Technology*, *48*(5), 552–561.

Ramanathan, V., P. J. Crutzen, J. T. Kiehl, and D. Rosenfeld (2001), Aerosols, Climate, and the Hydrological Cycle, *Science*, *294*(5549), 2119–2124.

Roberts, G. C., and A. Nenes (2005), A Continuous-Flow Streamwise Thermal-Gradient CCN Chamber for Atmospheric Measurements, *Aerosol Science and Technology*, *39*(3), 206–221.

Roberts, G. C., D. A. Day, L. M. Russell, E. J. Dunlea, J. L. Jimenez, J. M. Tomlinson, D. R. Collins, Y. Shinozuka, and A. D. Clarke (2010), Characterization of particle cloud droplet activity and composition in the free troposphere and the boundary layer during INTEX-B, *Atmospheric Chemistry and Physics*, *10*(14), 6627–6644.

Rose, D., S. S. Gunthe, E. Mikhailov, G. P. Frank, U. Dusek, M. O. Andreae, and U. Pöschl (2008), Calibration and measurement uncertainties of a continuous-flow cloud condensation nuclei counter (DMT-CCNC)- CCN activation of ammonium sulfate and sodium chloride aerosol particles in theory and experiment, *Atmospheric Chemistry and Physics*, *8*, 1153–1179.

Rose, D., A. Nowak, P. Achtert, A. Wiedensohler, M. Hu, M. Shao, Y. Zhang, M. O. Andreae, and U. Pöschl (2010), Cloud condensation nuclei in polluted air and biomass burning smoke near the mega-city Guangzhou, China - Part 1: Size-resolved measurements and implications for the modeling of aerosol particle hygroscopicity and CCN activity, *Atmospheric Chemistry and Physics*, *10*, 3365–3383.

Russell, L. M., A. Sorooshian, J. H. Seinfeld, B. A. Albrecht, A. Nenes, L. Ahlm, Y.-C. Chen, M. Coggon, J. S. Craven, R. C. Flagan, A. A. Frossard, H. Jonsson, E. Jung, J. J. Lin, A. R. Metcalf, R. Modini, J. Mülmenstädt, G. Roberts, T. Shingler, S. Song, Z. Wang, and A. Wonaschütz (2013), Eastern Pacific Emitted Aerosol Cloud Experiment, *Bulletin of the American Meteorological Society*, *94*(5), 709–729.

Samson, P. J., and B. Shi (1988), A meteorological investigation of high ozone values in American cities, a report to the Office of Technology Assessment, United States Government Printing Office, Washington, D.C.

Sareen, N., A. N. Schwier, T. L. Lathem, A. Nenes, and V. F. McNeill (2013), Surfactants from the gas phase may promote cloud droplet formation, *Proceedings of the National Academy of Sciences*, *110*(8), 2723–2728.

Schwarz, J. P., J. R. Spackman, D. W. Fahey, R. S. Gao, U. Lohmann, P. Stier, L. A. Watts, D. S. Thomson, D. A. Lack, L. Pfister, M. J. Mahoney, D. Baumgardner, J. C. Wilson, and J. M. Reeves (2008), Coatings and their enhancement of black carbon light absorption in the tropical atmosphere, *Journal of Geophysical Research*, *113*(D3), D03,203.

Schwarz, J. P., J. R. Spackman, R. S. Gao, L. A. Watts, P. Stier, M. Schulz, S. M. Davis, S. C. Wofsy, and D. W. Fahey (2010), Global-scale black carbon profiles observed in the remote atmosphere and compared to models, *Geophysical Research Letters*, *37*(18), n/a–n/a.

Seinfeld, J. H., and S. N. Pandis (2006), *Atmospheric Chemistry and Physics: From Air Pollution to Climate Change*, 2 ed., John Wiley & Sons, Inc., Hoboken.

Shulman, M. L., M. C. Jacobson, R. J. Charlson, R. E. Synovec, and T. E. Young (1996), Dissolution behavior and surface tension effects of organic compounds in nucleating cloud droplets, *Geophysical Research Letters*, *23*(3), 277–280.

Solomon, P. A., D. Crumpler, J. B. Flanagan, R. K. M. Jayanty, E. E. Rickman, and C. E. McDade (2014), United States National PM2.5Chemical Speciation Monitoring Networks – CSN and IMPROVE: Description of Networks, *Journal of the Air & Waste Management Association*, *64*(12), 1410–1438.

Sorjamaa, R., and A. Laaksonen (2007), The effect of H_2O adsorption on cloud drop activation of insoluble particles: a theoretical framework, *Atmospheric Chemistry and Physics*, *7*, 6175–6180.

Sorooshian, A., S. M. Murphy, S. Hersey, H. Gates, L. T. Padró, A. Nenes, F. J. Brechtel, H. Jonsson, R. C. Flagan, and J. H. Seinfeld (2008), Comprehensive airborne characterization of aerosol from a major bovine source, *Atmospheric Chemistry and Physics*, *8*, 5489–5520.

Stocker, T., D. Qin, G.-K. Plattner, L. Alexander, S. Allen, N. Bindoff, F.-M. Breòn, J. Church, U. Cubasch, S. Emori, P. Forster, P. Friedlingstein, N. Gillett, J. Gregory, D. Hartmann, E. Jansen, B. Kirtman, R. Knutti, K. Krishna Kumar, P. Lemke, J. Marotzke, V. Masson-Delmotte, G. Meehl, I. Mokhov, S. Piao, V. Ramaswamy, D. Randall, M. Rhein, M. Rojas, C. Sabine, D. Shindell, L. Talley, D. Vaughan, and S.-P. Xie (2013), *Technical Summary*, book section TS, pp. 33–115, Cambridge University Press, Cambridge, United Kingdom and New York, NY, USA, doi:10.1017/CBO9781107415324.005.

Tanner, R. L., S. T. Bairai, and S. F. Mueller (2015), Trends in concentrations of atmospheric gaseous and particulate species in rural eastern Tennessee as related to primary emission reductions, *Atmospheric Chemistry and Physics*, *15*(17), 9781–9797.

Twomey, S. (1974), Pollution and the Planetary Albedo, *Atmospheric Environment*, *8*, 1251–1256.

Twomey, S. (1977), Influence of Pollution on Shortwave Albedo of Clouds, *Journal of the Atmospheric Sciences*, *34*(7), 1149–1152.

Volkamer, R., J. L. Jimenez, F. San Martini, K. Dzepina, Q. Zhang, D. Salcedo, L. T. Molina, D. R. Worsnop, and M. J. Molina (2006), Secondary organic aerosol formation from anthropogenic air pollution: Rapid and higher than expected, *Geophysical Research Letters*, *33*(17).

Warneke, C., M. Trainer, J. A. de Gouw, D. D. Parrish, D. W. Fahey, A. R. Ravishankara, A. M. Middlebrook, C. A. Brock, J. M. Roberts, S. S. Brown, J. A. Neuman, B. M. Lerner, D. Lack, D. Law, G. Huebler, I. Pollack, S. Sjostedt, T. B. Ryerson, J. B. Gilman, J. Liao, J. Holloway, J. Peischl, J. B. Nowak, K. Aikin, K. E. Min, R. A. Washenfelder, M. G. Graus, M. Richardson, M. Z. Markovic, N. L. Wagner, A. Welti, P. R. Veres, P. Edwards, J. P. Schwarz, T. Gordon, W. P. Dube, S. McKeen, J. Brioude, R. Ahmadov, A. Bougiatioti, J. Lin, A. Nenes, G. M. Wolfe, T. F. Hanisco, B. H. Lee, F. D. Lopez-Hilfiker, J. A. Thornton, F. N. Keutsch, J. Kaiser, J. Mao, and C. Hatch (2016), Instrumentation and Measurement Strategy for the NOAA SENEX Aircraft Campaign as Part of the Southeast Atmosphere Study 2013, *Atmospheric Measurement Techniques Discussions*, pp. 1–39.

Weber, R. J., A. P. Sullivan, R. E. Peltier, A. Russell, B. Yan, M. Zheng, J. de Gouw, C. Warneke, C. Brock, J. S. Holloway, E. L. Atlas, and E. Edgerton (2007), A study of secondary organic aerosol formation in the anthropogenic-influenced southeastern United States, *Journal of Geophysical Research*, *112*(D13), n/a–n/a.

Wex, H., T. Hennig, I. Salma, R. Ocskay, A. Kiselev, S. Henning, A. Massling, A. Wiedensohler, and F. Stratmann (2007), Hygroscopic growth and measured and modeled critical super-saturations of an atmospheric HULIS sample, *Geophysical Research Letters*, *34*(2).

Xu, L., H. Guo, C. M. Boyd, M. Klein, A. Bougiatioti, K. M. Cerully, J. R. Hite, G. Isaacman-VanWertz, N. M. Kreisberg, C. Knote, K. Olson, A. Koss, A. H. Goldstein, S. V. Hering, J. de Gouw, K. Baumann, S.-H. Lee, A. Nenes, R. J. Weber, and N. L. Ng (2015), Effects of anthropogenic emissions on aerosol formation

from isoprene and monoterpenes in the southeastern United States, *Proceedings of the National Academy of Sciences*, *112*(1), 37–42.

Yu, S., R. Mathur, J. Pleim, D. Wong, R. Gilliam, K. Alapaty, C. Zhao, and X. Liu (2014), Aerosol indirect effect on the grid-scale clouds in the two-way coupled WRF–CMAQ: model description, development, evaluation and regional analysis, *Atmospheric Chemistry and Physics*, *14*(20), 11,247–11,285.

VITA

Jack Lin was born in Buffalo, New York, USA, in 1988 to Wei Lin and Xingguang Wang. He attended the California Institute of Technology, receiving a B.S. degree in chemical engineering in 2009. At Caltech, he was introduced to research in atmospheric sciences by Professors Richard C. Flagan, John H. Seinfeld, and Paul O. Wennberg. In 2009, he joined the research group of Professor Athanasios Nenes at the Georgia Institute of Technology to pursue a Ph.D. in Earth and Atmospheric Sciences. During his Ph.D. research, he participated in eight airborne field measurement campaigns. Jack was supported in part by a NASA Graduate Student Researchers Project Fellowship and a Georgia Institute of Technology President's Fellowship. He is a co-author of nine peer-reviewed journal articles and the author of two publications in review or preparation. He will graduate with a Ph.D. in May 2016.